Earth-Science Reviews 140 (2015) 108–157

Contents lists available at ScienceDirect

Earth-Science Reviews

journal homepage: www.elsevier.com/locate/earscirev

Aerosol remote sensing in polar regions

Claudio Tomasi [a,*], Alexander A. Kokhanovsky [b,c], Angelo Lupi [a], Christoph Ritter [d], Alexander Smirnov [e,f], Norman T. O'Neill [g], Robert S. Stone [h,i], Brent N. Holben [f], Stephan Nyeki [j], Christoph Wehrli [j], Andreas Stohl [k], Mauro Mazzola [a], Christian Lanconelli [a], Vito Vitale [a], Kerstin Stebel [k], Veijo Aaltonen [l], Gerrit de Leeuw [l,m], Edith Rodriguez [l], Andreas B. Herber [n], Vladimir F. Radionov [o], Tymon Zielinski [p], Tomasz Petelski [p], Sergey M. Sakerin [q], Dmitry M. Kabanov [q], Yong Xue [r,s], Linlu Mei [s], Larysa Istomina [b], Richard Wagener [t], Bruce McArthur [u,1], Piotr S. Sobolewski [v], Rigel Kivi [w], Yann Courcoux [x], Pierre Larouche [y], Stephen Broccardo [z], Stuart J. Piketh [aa]

[a] Climate Change Division, Institute of Atmospheric Sciences and Climate (ISAC), Italian National Research Council (CNR), Bologna, Italy
[b] Institute of Environmental Physics (IUP), University of Bremen, Bremen, Germany
[c] EUMETSAT, Eumetsat Allee 1, D-64295 Darmstadt, Germany
[d] Climate System Division, Alfred Wegener Institute for Polar and Marine Research, Potsdam, Germany
[e] Sigma Space Corporation, Lanham, MD, USA
[f] Biospheric Sciences Branch, NASA/Goddard Space Flight Center (GSFC), Greenbelt, MD, USA
[g] Canadian Network for the Detection of Atmospheric Change (CANDAC) and CARTEL, Dept. of Applied Geomatics, University of Sherbrooke, Sherbrooke, Québec, Canada
[h] Global Monitoring Division (GMD), National Oceanic and Atmospheric Administration (NOAA), Boulder, CO, USA
[i] Cooperative Institute for Research in Environmental Sciences (CIRES), University of Colorado, Boulder, CO, USA
[j] Physikalisch-Meteorologisches Observatorium (PMOD)/World Radiation Centre (WRC), Davos, Switzerland
[k] Norwegian Institute for Air Research (NILU), Kjeller, Norway
[l] Climate and Global Change Division, Finnish Meteorological Institute (FMI), Helsinki, Finland
[m] Department of Physics, University of Helsinki, Finland
[n] Climate System Division, Alfred Wegener Institute for Polar and Marine Research, Bremerhaven, Germany
[o] Arctic and Antarctic Research Institute (AARI), St. Petersburg, Russia
[p] Institute of Oceanology (IO), Polish Academy of Sciences (PAS), Sopot, Poland
[q] V. E. Zuev Institute of Atmospheric Optics (IAO), Siberian Branch (SB), Russian Academy of Sciences (RAS), Tomsk, Russia
[r] Faculty of Life Sciences and Computing, London Metropolitan University, London, United Kingdom
[s] Key Laboratory of Digital Earth Science, Institute of Remote Sensing and Digital Earth, Chinese Academy of Sciences, Beijing 100094, China
[t] Brookhaven National Laboratory, Environmental and Climate Sciences Dept Upton, NY, USA
[u] Environment Canada, Downsview, North York, Ontario, Canada
[v] Institute of Geophysics, Polish Academy of Sciences (PAS), Warsaw, Poland
[w] Arctic Research Center, Finnish Meteorological Institute (FMI), Sodankylä, Finland
[x] Institute de l'Atmosphère de la Réunion (OPAR), Univ. de la Réunion, CNRS, Saint Denis de la Réunion, France
[y] Institut Maurice-Lamontagne, Mont-Joli, Quebec, Canada
[z] Geography, Archeology and Environmental Science, University of the Witwatersrand, Johannesburg, South Africa
[aa] Climatology Research Group, Unit for Environmental Sciences and Management, North-West University, Potchefstroom, South Africa

ARTICLE INFO

Article history:
Received 15 April 2014
Accepted 1 November 2014
Available online 10 November 2014

Keywords:
Sun-photometer measurements
Aerosol optical thickness
Polar aerosol optical characteristics
Lidar backscattering coefficient profiles
Satellite aerosol remote sensing
Multimodal aerosol extinction models

ABSTRACT

Multi-year sets of ground-based sun-photometer measurements conducted at 12 Arctic sites and 9 Antarctic sites were examined to determine daily mean values of aerosol optical thickness $\tau(\lambda)$ at visible and near-infrared wavelengths, from which best-fit values of Ångström's exponent α were calculated. Analysing these data, the monthly mean values of $\tau(0.50\ \mu m)$ and α and the relative frequency histograms of the daily mean values of both parameters were determined for winter–spring and summer–autumn in the Arctic and for austral summer in Antarctica. The Arctic and Antarctic covariance plots of the seasonal median values of α versus $\tau(0.50\ \mu m)$ showed: (i) a considerable increase in $\tau(0.50\ \mu m)$ for the Arctic aerosol from summer to winter–spring, without marked changes in α; and (ii) a marked increase in $\tau(0.50\ \mu m)$ passing from the Antarctic Plateau to coastal sites, whereas α decreased considerably due to the larger fraction of sea-salt aerosol. Good agreement was found when comparing ground-based sun-photometer measurements of $\tau(\lambda)$ and α at Arctic and Antarctic coastal sites with Microtops measurements conducted during numerous AERONET/MAN cruises from 2006 to 2013 in three Arctic

* Corresponding author. Tel.: +39 051 639 9594; fax: +39 051 639 9652.
E-mail address: c.tomasi@isac.cnr.it (C. Tomasi).
[1] Now with Agriculture and Agri-food Canada.

http://dx.doi.org/10.1016/j.earscirev.2014.11.001

Ocean sectors and in coastal and off-shore regions of the Southern Atlantic, Pacific, and Indian Oceans, and the Antarctic Peninsula.

Lidar measurements were also examined to characterise vertical profiles of the aerosol backscattering coefficient measured throughout the year at Ny-Ålesund. Satellite-based MODIS, MISR, and AATSR retrievals of $\tau(\lambda)$ over large parts of the oceanic polar regions during spring and summer were in close agreement with ship-borne and coastal ground-based sun-photometer measurements. An overview of the chemical composition of mode particles is also presented, based on in-situ measurements at Arctic and Antarctic sites. Fourteen log-normal aerosol number size-distributions were defined to represent the average features of nuclei, accumulation and coarse mode particles for Arctic haze, summer background aerosol, Asian dust and boreal forest fire smoke, and for various background austral summer aerosol types at coastal and high-altitude Antarctic sites. The main columnar aerosol optical characteristics were determined for all 14 particle modes, based on in-situ measurements of the scattering and absorption coefficients. Diurnally averaged direct aerosol-induced radiative forcing and efficiency were calculated for a set of multimodal aerosol extinction models, using various Bidirectional Reflectance Distribution Function models over vegetation-covered, oceanic and snow-covered surfaces. These gave a reliable measure of the pronounced effects of aerosols on the radiation balance of the surface–atmosphere system over polar regions.

Contents

1. Introduction

Aerosols are one of the greatest sources of uncertainty in climate modelling, as their microphysical, chemical and optical characteristics as well as their concentration vary in time and in space, inducing significant direct radiative forcing effects on the surface–atmosphere system. In addition, they can alter cloud optical features and indirectly impact climate. The aim of this paper is to present an overview of the optical characteristics of atmospheric aerosol observed in polar regions during the past two decades, including recent measurements conducted with ground-based and ship-borne sun-photometers, or retrieved from remote sensing data recorded with visible and infrared sensors mounted onboard various satellite platforms. Optical instruments (e.g., lidars, sun-photometers) measure the characteristics of the atmospheric light field (internal, reflected, or transmitted). Specific procedures therefore need to be applied to convert optical signals to aerosol characteristics, such as particle size and shape distributions, or chemical composition. Similar procedures are also needed to derive the vertical concentration distribution from columnar measurements. They are based on the solution of the inverse problem of radiative transfer theory accounting for multiple light scattering, molecular and aerosol scattering and absorption, and surface reflectance effects.

The presence of a visibility-reducing haze in the Arctic was already noted by early explorers in the 19th century (see Garrett and Verzella, 2008, for a historical overview). The explorers also documented that haze particles were deposited on snow in remote parts of the Arctic (e.g., Nordenskiöld, 1883) and haze layers were also observed later by pilots in the 1950s (Mitchell, 1957). The source of the haze was debated for almost a century but poorly understood until the 1970s when it was suggested that this “Arctic Haze” originated from emissions in northern mid-latitudes and was transported into the Arctic over thousands of kilometres (Rahn et al., 1977; Barrie et al., 1981). The seasonality of the haze, which peaks in winter and early spring, was explained by the fact that removal processes are inefficient in the Arctic during that time of the year (Shaw, 1995).

Polar aerosols originate from both natural and anthropogenic sources (Shaw, 1988, 1995). In the Arctic regions, natural aerosols have been found to contain an oceanic sea-salt mass fraction that frequently

exceeds 50% on summer days, and a mass fraction of 30–35% due to mineral dust, with lower percentages of non-sea-salt (nss) sulphate, methane sulphonic acid (MSA), and biomass burning combustion products. In contrast, anthropogenic particles have higher concentrations of sulphates, organic matter (OM) and black carbon (BC) with respect to natural aerosol (Quinn et al., 2002, 2007; Sharma et al., 2006). In fact, boreal forest fire (hereinafter referred to as BFF) smoke transported from North America and Siberia often contributes to enhance soot concentration in summer (Damoah et al., 2004; Stohl et al., 2006). Rather high aerosol mass concentrations of anthropogenic origin are frequently transported from North America and especially Eurasia in the winter and spring months, leading to intense Arctic haze episodes (Shaw, 1995). For instance, Polissar et al. (2001) conducted studies on the BC source regions in Alaska from 1991 to 1999 finding that predominant contributions have been given by large-scale mining and industrial activities in South and Eastern Siberia. In the North European sector of the Arctic, the dominant sources of sulphates and nitrates (and to a lesser extent of water-soluble OM and BC) are located in Europe and Siberia, due to both urban pollution and industrial activities (Hirdman et al., 2010). Episodes of Asian dust transport have also been observed over the past years in the North American sector of the Arctic, especially in spring (Stone et al., 2007), together with local transport of soil particles mobilised by strong winds, which provisionally enhance the mass concentrations of elemental components, such as Al, Si, Mg and Ca (Polissar et al., 1998). The Arctic atmosphere's stratification is highly stable, with frequent and strong inversions near the surface, which limit turbulence and reduce the dry deposition of aerosols to the surface (Strunin et al., 1997). They also decouple the sea ice inversion layer from the Arctic free troposphere, leading to very different chemical and physical properties of aerosols in the sea ice inversion layer where aerosols are depleted, and higher up where a sulphate-rich background aerosol typically of anthropogenic origin is often found (Brock et al., 2011). In addition, organic-rich biomass burning layers occur in the free troposphere but rarely reach the surface (Warneke et al., 2010; Brock et al., 2011). The low-altitude high-latitude atmosphere in the southern hemisphere is similarly stably stratified as in the Arctic's but is also influenced strongly by katabatic winds bringing down air from the high altitudes of interior Antarctica (Stohl and Sodemann, 2010).

On larger scales, the stable Arctic stratification leads to the so-called polar dome, where isentropes form shells above the Arctic. As atmospheric transport tends to follow the isentropes, direct transport of air masses from mid-latitude pollution source regions into the Arctic lower troposphere is very inefficient. According to Stohl (2006), polluted air masses from lower latitudes typically follow one of five major transport pathways (see Fig. 1): (1) lifting at the Arctic front, where wet scavenging is efficient; (2) lifting at lower latitudes (at the polar front or convection), where wet scavenging is even more efficient; (3) most importantly for Arctic surface aerosol concentrations, low-level transport over land in winter where strong radiative cooling allows air masses to enter the polar dome; (4) slow descent by radiative cooling of upper-tropospheric air masses into the polar dome; (5) slow mixing across the lateral boundaries of the dome. Forest or agricultural fires are important, as they produce strong aerosol plumes in the mid- to high-latitude free troposphere, which can subsequently enter the Arctic by one of the previously mentioned processes.

In addition to long-range pollution transport, local emission sources can be important. For instance, emissions from cruise ships can lead to measurable enhancements of BC and other aerosols in the Svalbard archipelago (Eckhardt et al., 2013). Diesel generators can also locally pollute the environment (Hagler et al., 2008). Aircraft emissions north of the Arctic circle are primarily injected into the stratosphere where removal is inefficient and these emissions can slowly descend (Whitt et al., 2011). All these local sources can also enhance the Arctic aerosol background; however, quantification of their contribution relative to long-range transport of pollution from sources outside the Arctic remains uncertain. In addition, sulphate and volcanic ash from high-latitude eruptions can occasionally influence the Arctic troposphere (e.g., Hoffmann et al., 2010). The stratospheric background aerosol in the Arctic as elsewhere can be perturbed by explosive volcanic eruptions (especially in the tropics) for several years. Some volcanic aerosol emission episodes have been observed by Bourassa et al. (2010) and O'Neill et al. (2012) over the last few years, involving the low stratosphere over short periods of a few months.

Transport processes in the high-latitude southern hemisphere are similar to those sketched for the Arctic in Fig. 1. As in the northern hemisphere, polluted air masses from the lower-latitude continents are quasi-isentropically lifted to higher altitudes and, furthermore, there is no low-altitude transport pathway over land in winter (i.e., the analogue to transport pathway number 3 in Fig. 1 is missing in the southern hemisphere). Consequently, as in the Arctic, the lowermost troposphere in the Antarctic is very isolated and, thus, contains little anthropogenic pollution transported from lower-latitude continents (Stohl and Sodemann, 2010). A major difference to the Arctic, however, is the high topography of the Antarctic continent. This means that the most isolated air masses (as measured by the time since last exposure to pollution sources at lower-latitude continents) are not found close to the pole, as in the Arctic, but in the coastal areas surrounding Antarctica (Stohl and Sodemann, 2010). Descent over the Antarctic continent is stronger than over the Arctic and can also bring down air from the stratosphere, and air from the Antarctic interior is transported down to coastal areas by strong katabatic winds.

In Antarctica, aerosols sampled at coastal sites originate almost totally from natural processes, with a prevailing oceanic sea-salt mass content of 55–60%, and lower percentages of nss sulphate (20–30%)

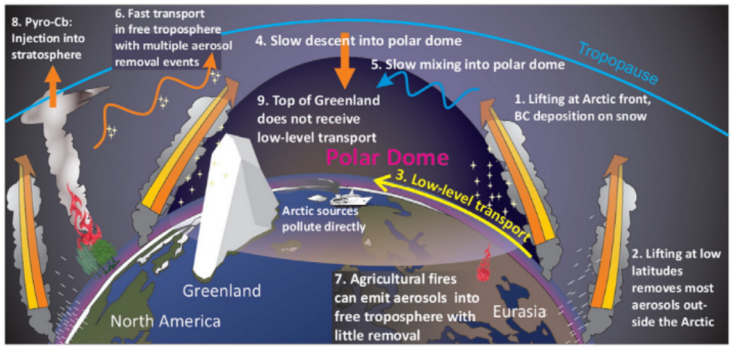

Fig. 1. Schematic of the main transport pathways of aerosols into the Arctic, as described by Law et al. (in press) [used with permission of the American Meteorological Society].

and mineral dust (10–20%) (Tomasi et al., 2012). Only very low mass fractions of nitrates, water-soluble OM and BC have been monitored in Antarctica, mainly associated with transport from remote anthropogenic sources (Wolff and Cachier, 1998) or biomass burning (Fiebig et al., 2009) in mid-latitude areas. More than 60–80% of particulate matter suspended over the Antarctic Plateau has been estimated to consist of nss sulphates formed from biogenic sulphur compounds and/or MSA, due to long-range transport in the free troposphere and subsequent subsidence processes. Therefore, aerosols sampled at these high-altitude sites contain only moderate mass fractions of nitrates, and minor or totally negligible mass percentages of mineral dust, water-soluble OM and BC (Tomasi et al., 2007, 2012).

The paper is organised as follows. In the next section the ground-based remote sensing measurements of atmospheric aerosol are reviewed (sun-photometers, lidars). Section 3 gives a description of ship-borne aerosol remote sensing instruments. Section 4 discusses aerosol backscattering coefficient profiles from lidar measurements, while Section 5 is dedicated to airborne and satellite observations of polar aerosols. The last section presents the most important optical characteristics and size-distribution features of polar aerosols, which are appropriate for calculations of direct radiative forcing effects induced by aerosols on the climate system.

2. Ground-based remote sensing measurements

2.1. Spectral measurements of aerosol optical thickness

Ground-based remote sensing of the optical characteristics of aerosols in the atmospheric column is usually conducted with multi-wavelength sun-photometers. A sun-photometer is oriented towards the Sun to detect the solar radiation attenuated along the slant path from the top-of-atmosphere (TOA) to the ground. The atmospheric aerosol load leads to a decrease in the solar radiation transmitted through the atmosphere. This decrease depends on the aerosol optical thickness (hereinafter referred to as AOT and/or using symbol $\tau(\lambda)$), which is given by the integral of the volume aerosol extinction coefficient along the vertical path of the atmosphere.

The networks, sites and sun-photometers whose data were employed in this paper are defined and characterised in Tables 1 and 2 for the Arctic and Antarctic regions, respectively. The largest networks of sun-photometers in the world are AERONET and SKYNET. Spectral measurements of $\tau(\lambda)$ are performed with AERONET sun-photometers (Holben et al., 1998) at 8 wavelengths ranging from 0.340 to 1.600 μm, and with SKYNET instruments (Nakajima et al., 2007) at 10 wavelengths from 0.315 to 2.200 μm. The Cimel CE-318 sun-photometers of the AERONET network are currently used at several Arctic sites: Barrow (since March 2002), Thule (since March 2007), Hornsund (since April 2005), Sodankylä (since February 2007), Tiksi (since June 2010), Resolute Bay (since July 2004), Eureka-0PAL (since April 2007) and Eureka-PEARL (since May 2007). The last three sites, located in the Nunavut region of Canada, are part of the AEROCAN/AERONET network. In addition, an AERONET sun-photometer has been intermittently used since 2002 by the Atmospheric Optics Group (GOA) (University of Valladolid, Spain) at the Arctic Lidar Observatory for Middle Atmosphere Research (ALOMAR), located on the Andøya Rocket Range, near Andenes (Northern Norway) (Toledano et al., 2012). AERONET sun-photometers have been used to obtain Level 2.0 $\tau(\lambda)$ measurements at the South Pole (since November 2007), and occasionally at Dome Concordia (in January and December 2003) in Antarctica. AERONET Level 1.5 measurements of $\tau(\lambda)$ are available for McMurdo on the Ross Sea (from February to December 1997, in the austral summer 2001/2002, and in January–February 2011), at Marambio (Antarctic Peninsula) since October 2007, at Vechernaya Hill (Thala Hills, Enderby Land) since December 2008, and at Utsteinen (Dronning Maud Land) since February 2009. However, because these data were not promoted to Level 2.0, they were not considered in the present study. A PREDE POM-01L sun/sky radiometer was used in Antarctica during the 2001–2002 austral summer by Di Carmine et al. (2005) at the Mario Zucchelli station. PREDE instruments have been used since 2001 in Antarctica at Syowa (East Ongul Island, Lützow-Holm Bay) by the National Institute of Polar Research (NIPR, Tokyo, Japan) since 2001, at Rothera by the British Antarctic Survey (BAS) since January 2008, and at Halley by BAS since February 2009. In addition, Precision Filter Radiometer (PFR) sun-photometers (Wehrli, 2000; Nyeki et al., 2012) from the Global Atmosphere Watch (GAW) PFR network are currently used in the Arctic at Summit by PMOD/WRC (Switzerland), at Ny-Ålesund by NILU (Norway), and at Sodankylä by FMI (Finland), and in Antarctica at Marambio by FMI and at Troll by NILU. The instrumental and geometrical characteristics of the PFR sun-photometer are described by Wehrli (2000).

The monochromatic total optical thickness $\tau_{TOT}(\lambda)$ of the atmosphere is commonly calculated in terms of the well known Lambert–Beer law for a certain sun-photometer output voltage $J(\lambda)$ taken within a spectral channel centred at wavelength λ and for a certain apparent solar zenith angle θ_0. The monochromatic value of $\tau_{TOT}(\lambda)$ is given by (Shaw, 1976):

$$\tau_{TOT}(\lambda) = m \ln\left[R J_0(\lambda) / J(\lambda)\right] \quad (1)$$

where: (i) m is the relative optical air mass calculated as a function of θ_0 using a realistic model of the atmosphere, in which wet-air refraction and Earth/atmosphere curvature effects on the direct solar radiation passing through the atmosphere are properly taken into account (Thomason et al., 1983; Tomasi and Petkov, 2014); (ii) $J(\lambda)$ is the output signal (proportional to solar irradiance) measured by the ground-based solar pointing sun-photometer; (iii) $J_0(\lambda)$ is the output signal that would be measured by the sun-photometer outside the terrestrial atmosphere, at the mean Earth–Sun distance; and (iv) R accounts for $J_0(\lambda)$ variations as a function of the daily Earth–Sun distance (Iqbal, 1983).

The solar radiation reaching the surface for cloud-free sky conditions is attenuated not only by aerosol extinction but also by Rayleigh scattering (Tomasi et al., 2010) as well as absorption by minor gases (mainly water vapour (H_2O), ozone (O_3), nitrogen dioxide (NO_2) and its dimer (N_2O_4), and oxygen dimer (O_4)). The spectral values of $\tau(\lambda)$ within the main windows of the atmospheric transmission spectrum are accordingly calculated by subtracting the Rayleigh scattering and absorption optical thicknesses from $\tau_{TOT}(\lambda)$.

AOT is usually a smooth function of wavelength λ (measured in μm), which can be approximated by the following simple formula:

$$\tau(\lambda) = \tau(\lambda_0)(\lambda/\lambda_0)^{-\alpha}; \quad (2)$$

where α is the so-called Ångström (1964) wavelength exponent, and λ_0 is usually assumed to be equal to 1 μm. In reality, the analytical form defined in Eq. (2) can be convex or concave depending on the relative contents of fine and coarse particles in the atmospheric column. O'Neill et al. (2001a) demonstrated that the variation in $\tau(\lambda)$ and its first and second spectral derivatives (named here α and α', respectively) can be realistically described in terms of the spectral interaction between the individual optical components of a bimodal size-distribution. O'Neill et al. (2001a) then showed that one can exploit the spectral curvature information in the measured $\tau(\lambda)$ to permit a direct estimate of a fine mode Ångström exponent (α_f) as well as the optical fraction of fine mode particles. However, an analysis of α and α' determined in real cases and taking into account that both α(0.44–0.87 μm) and α' are closely related to the spectral features of $\tau(\lambda)$ showed that propagation of errors leads to an error $\Delta\alpha/\alpha \sim 2\,\Delta\tau(\lambda)/\tau(\lambda)$ and an error $\Delta\alpha'/\alpha' \sim 5\Delta\tau(\lambda)/\tau(\lambda)$, respectively (Gobbi et al., 2007). These estimates yield values of $\Delta\alpha/\alpha$ and $\Delta\alpha'/\alpha'$ that are ≥20% and ≥50%, respectively, for $\tau(\lambda) \leq 0.10$ and a typical sun-photometry error equal to ~0.01. To avoid relative errors ≥30% in

Table 1
List of the Arctic stations, where regular ground-based sun-photometer measurements have been conducted over the past decades, using different instrument models equipped with a variable number of narrow-band interference filters to determine the spectral values of aerosol optical thickness $\tau(\lambda)$ and Ångström wavelength exponent α in the visible and near-infrared wavelength range.

Sun-photometer stations	Managing institutions	Geographical coordinates and altitude	Overall number of measurement days	Measurement period	Sun-photometer model	Peak wavelengths (nm) of the spectral channels	Spectral interval (nm) of α	References
Barrow, Alaska (USA)	GMD/NOAA, Boulder, Colorado, USA	71° 19′ N, 156° 36′ W, 8 m a.m.s.l.	832 (cloud-screened by GMD/NOAA)	March 2000–September 2012	Carter Scott SP02 Carter Scott SP01-A Carter Scott SP022	412, 500, 675, 862 367, 610, 778, 1050 368, 610, 778, 1050	412–862 367–778 368–778	Stone (2002)
Barrow, Alaska (USA)	AERONET, NASA/GSFC, (Greenbelt, Maryland, USA); U.S. DoE Atmospheric Radiation Measurement Program, USA	71° 19′ N, 156° 40′ W, 0 m a.m.s.l.	579 (Level 2.0)	March 2002–September 2013	Cimel CE-318	340, 380, 440, 500, 675, 870, 1020, 1640	440–870	Holben et al. (1998)
Resolute Bay, Nunavut (Canada)	AERONET/AEROCAN, Environment Canada, Downsview, Ontario, Canada	74° 44′ N, 94° 54′ W, 40 m a.m.s.l.	361 (Level 2.0)	July 2004–October 2012	Cimel CE-318	340, 380, 440, 500, 675, 870, 1020, 1640	440–870	
Eureka-0PAL, Nunavut (Canada)	AERONET/AEROCAN, CARTEL, University of Sherbrooke, Canada	79° 59′ N, 85° 56′ W, 0 m a.m.s.l.	360 (Level 2.0)	April 2007–September 2011	Cimel CE-318	340, 380, 440, 500, 675, 870, 1020, 1640	440–870	
Alert, Ellesmere Island, Nunavut (Canada)	GMD/NOAA, Boulder, Colorado, USA	82° 28′ N, 62° 30′ W, 210 m a.m.s.l.	810 (cloud-screened by GMD/NOAA)	August 2004–September 2012	Carter Scott SP02	412, 500, 675, 862, or 368, 610, 778, 1050	412–862 or 368–778	Stone (2002)
Thule, NW Greenland	AERONET, NASA/GSFC, Greenbelt, Maryland, USA	76° 31′ N, 68° 46′ W, 225 m a.m.s.l.	605 (Level 2.0)	March 2007–September 2012	Cimel CE-318	380, 440, 500, 675, 870, 1020	440–870	Holben et al. (1998)
Summit, Central Greenland	PMOD/WRC, Davos, Switzerland	72° 35′ N, 38° 28′ W, 3250 m a.m.s.l.	391 (cloud-screened by PMOD/WRC)	January 2001–October 2011	PFR#34	368, 412, 500, 862	412–862	Wehrli (2000)
Ittoqqortoormiit, Eastern Greenland	AERONET, NASA/GSFC, Greenbelt, Maryland, USA	70° 29′ N, 21° 57′ W, 68 m a.m.s.l.	307 (Level 2.0)	May 2010–October 2013	Cimel CE-318	340, 380, 440, 500, 675, 870, 1020	440–870	Holben et al. (1998)
Ny-Ålesund, Spitsbergen (Svalbard, Norway)	AWI, Bremerhaven, Germany	78° 54′ N, 11° 53′ E, 5 m a.m.s.l.	749 (cloud-screened by AWI)	April 2000–September 2013	SP1A SP2H STAR01	371, 380, 416, 443, 500, 532, 609, 675, 778, 864, 1025, 1046, 1062 367, 380, 413, 441, 501, 531, 605, 673, 776, 862, 1023, 1045 390, 441, 501, 531, 605, 673, 776, 862	443–864 441–862 441–862	Herber et al. (2002)
Ny-Ålesund, Spitsbergen (Svalbard, Norway)	NILU, Kjeller, Norway	78° 54′ N, 11° 53′ E, 5 m a.m.s.l.	693 (cloud-screened by NILU)	March 2002–September 2004, and March 2006–September 2013	PFR#18	367.7, 411.9, 500.6, 862.5	411.9–862.5	Wehrli (2000)
Barentsburg, Spitsbergen (Svalbard, Norway)	IAO-SB-RAS, Tomsk, Russia	78° 04′ N, 14° 13′ E, 20 m a.m.s.l.	56 (cloud-screened by IAO)	April–August of 2011 and 2012	New portable SPM	339, 380, 442, 500, 547, 675, 871, 1020, 1240, 1553, 2134	442–871	Sakerin et al. (2009, 2012, 2014)
Hornsund, Spitsbergen (Svalbard, Norway)	AERONET, NASA/GSFC, Greenbelt, Maryland, USA; Institute of Geophysics, PAS, Warsaw, Poland	77° 00′ N, 15° 34′ E, 10 m a.m.s.l.	514 (Level 2.0)	April 2005–August 2013	Cimel CE-318	380, 440, 500, 675, 870, 1020	440–870	Holben et al. (1998)
Sodankylä, Northern Finland	FMI, Helsinki, Finland	67° 22′ N, 26° 38′ E, 184 m a.m.s.l.	312 (cloud-screened by FMI)	May 2004–September 2013	PFR#32	367.6, 411.4, 500.5, 861.6	411.4–861.6	Wehrli (2000)
Sodankylä, Northern Finland	AERONET, NASA/GSFC, Greenbelt, Maryland, USA; FMI, Helsinki, Finland	67° 22′ N, 26° 38′ E, 184 m a.m.s.l.	119 (Level 2.0)	February 2007–November 2013	Cimel CE-318	340, 380, 440, 500, 675, 870, 1020, 1640	440–870	Holben et al. (1998)
Tiksi, Northern-Central Siberia (Russia)	AERONET, NASA/GSFC, Greenbelt, Maryland, USA	71° 35′ N, 128° 55′ E, 0 m a.m.s.l.	162 (Level 2.0)	June–October of 2010, 2011 and 2012	Cimel CE-318	340, 380, 440, 500, 675, 870, 1020	440–870	Holben et al. (1998)

Table 2
List of the coastal and high-altitude Antarctic stations, where regular ground-based sun-photometer measurements have been conducted over the two past decades, using different instrument models equipped with a variable number of narrow-band interference filters to determine the spectral values of background aerosol optical thickness $\tau(\lambda)$ and Ångström wavelength exponent α in the visible and near-infrared wavelength range.

Sun-photometer stations	Managing institutions	Geographical coordinates and altitude	Overall number of measurement days	Measurement period	Sun-photometer model	Peak wavelengths (nm) of the aerosol spectral channels	Spectral interval (nm) of α	References
Marambio, Seymour-Marambio Island	FMI, Heksinki, Finland	64° 14′ S, 56° 37′ W, 205 m a.m.s.l.	139 (cloud-screened by FMI)	August 2011–March 2013	PFR #29	367.6, 411.4, 500.5, 861.6	367.6–861.6	Wehrli (2000)
Neumayer, Weddell Sea coast	AWI, Bremerhaven, Germany	70° 39′ S, 8° 15′ W, 40 m a.m.s.l.	234 (cloud-screened by AWI)	September 2000–April 2007	SP1A	371, 380, 416, 443, 500, 532, 609, 675, 778, 864, 1025, 1046, 1062	443–864	Herber et al. (2002)
					SP2H	367, 380, 413, 441, 501, 531, 605, 673, 776, 862, 1023, 1045	441–862	
					STAR01	390, 441, 501, 531, 605, 673, 776, 862	441–862	
Troll, Queen Maud Land	NILU, Kjeller, Norway	72° 01′ S, 2° 32′ E, 1309 m a.m.s.l.	547 (cloud-screened by NILU)	January 2007–April 2013	PFR#40	368.7, 411.9, 500.6, 862.5	411.9–862.5	Wehrli (2000)
					PFR#42	368.9, 412.1, 499.7, 862.2	412.1–862.2	
Novolazarevskaya, Queen Maud Land	AARI, San Petersburg, Russia; AERONET, NASA/GSFC, Greenbelt, Maryland, USA.	70° 46′ S, 11° 50′ E, 119 m a.m.s.l.	83 (Level 1.5, cloud-screened by NASA/GSFC	December 2008–February 2009; November 2009–February 2010	Hand-held Microtops, calibrated at GSFC	440, 500, 675, 870	440–870	Smirnov et al. (2009)
Mirny, Davis Sea coast	AARI, St. Petersburg, Russia	66° 33′ S, 93° 01′ E, 40 m a.m.s.l.	725 (ABAS and SPM data cloud-screened by AARI; Microtops data cloud-screened using the Smirnov et al. (2009) procedure)	March 2000–October 2013	ABAS	395, 408, 479, 581, 651, 789, 873, 1041	408–873	Radionov et al. (2002), Radionov (2005)
					SPM	340, 379, 443, 499, 548, 676, 871, 1019, 1244, 1555, 2134	443–871	Sakerin et al. (2009, 2012), Tomasi et al. (2012)
					Microtops	440, 500, 675, 870	440–870	Smirnov et al. (2009)
Syowa, East Ongul Island, Lützow-Holm Bay	Japan Meteorological Agency (JMA), Tokyo, Japan	69° 00′ S, 39° 35′ E, 21 m a.m.s.l.	987 (cloud-screened by JMA)	January 2000–December 2011	EKO MS-110 model (with 2.5° field-of-view diameter)	368, 500, 675, 778, 862	368–862	Ohno (2005)
Mario Zucchelli, Terra Nova Bay, Ross Sea coast, Victoria Land	ISAC-CNR, Bologna, Italy	74° 42′ S, 164° 07′ E, 15 m a.m.s.l.	87 (cloud-screened by ISAC-CNR)	November 2001–February 2002	Prede POM-01L	400, 500, 675, 870, 1020	400–870	Di Carmine et al. (2005)
				December 2005–February 2006	ASP-15WL	381, 412, 451, 500, 551, 610, 673, 775, 861, 1026	412–861	Tomasi et al. (2007)
Dome Concordia, East Antarctic Plateau	AERONET, NASA/GSFC, Greenbelt, Maryland, USA	75° 05′ S, 123° 18′ E, 3260 m a.m.s.l.	44 (Level 1.5 data, cloud-screened by NASA/GSFC)	January and December 2003; January 2004	Cimel CE-318	440, 675, 870, 1020	440–870	Holben et al. (1998), Six et al. (2005)
	GMD/NOAA, Boulder, Colorado, USA	75° 06′ S, 123° 21′ E, 3233 m a.m.s.l.	65 (cloud-screened by GMD/NOAA)	January 2006–November 2010	Carter Scott SP02	412, 500, 675, 862	412–862	Stone (2002)
	OPAR Institute, (Univ. de la Réunion - CNRS, Saint Denis de la Réunion, France), and NASA/GSFC, (Greenbelt, Maryland, USA)	75° 05′ E, 123° 18′ E, 3260 m a.m.s.l.	39 (Level 1.5 data, cloud-screened by NASA/GSFC)	January, 2010, 2011, and 2012	Hand-held Microtops calibrated at the NASA/GSFC Facility	379, 441, 674, 868	441–868	Smirnov et al. (2011)
South Pole, Antarctic Plateau	GMD/NOAA, Boulder, Colorado, USA	90° 00′ S, 00° 00′ E, 2835 m a.m.s.l.	1279 (cloud-screened by GMD/NOAA)	November 2001–March 2012	Carter Scott SP02	412, 500, 675, 862	412–862	Stone (2002)
	AERONET, NASA/GSFC, Greenbelt, Maryland, USA; GMD/NOAA, Boulder, Colorado, USA	89° 59′ S, 70° 18′ E, 2850 m a.m.s.l.	147 (Level 2.0 data, cloud-screened by NASA/GSFC)	November 2007–December 2012	Cimel CE-318	340, 380, 440, 500, 675, 870, 1020	440–870	Holben et al. (1998)

$\Delta\alpha'/\alpha'$, Gobbi et al. (2007) suggested using only observations of $\tau(\lambda)$ N 0.15. We applied the same criterion as a threshold for accepting outputs from the Spectral Deconvolution Algorithm (SDA) of O'Neill et al. (2003) (notably the fine mode Ångström exponent, which offers an alternative refinement to the calculation of α): our logic being that α and α' are input parameters to SDA and we did not want to introduce unacceptable processing errors to the extraction of a spectral exponent indicator. These limitations to the use of spectral values of α and α' were also applied by Yoon et al. (2012), who only considered observations with $\tau(0.44\ \mu m)$ N 0.15 in order to avoid relative errors N30% in α'. Tomasi et al. (2007) showed that for the period 1977–2006, $\tau(0.50\ \mu m)$ did not exceed 0.15 for background summer aerosol conditions at Barrow, Alert, Summit, Ny-Ålesund, Hornsund, Sodankylä and Andenes/ALOMAR in the Arctic, and was greater than 0.15 only during very strong episodes of Arctic haze in late winter and spring, and BFF smoke transport in summer. Similarly, Tomasi et al. (2012) found that (i) the measurements of $\tau(0.50\ \mu m)$ recorded from 2000 to 2012 at Ny-Ålesund were estimated to exceed 0.15 in summer (June to September) in only a few cases of strong transport of BFF smoke from lower latitudes; even in winter (December to March), they were higher than 0.15 only for 10% of the cases, typically associated with Arctic haze transport episodes; (ii) measurements of $\tau(0.50\ \mu m)$ N 0.15 recorded at Barrow over the same period were observed only in a few percent of cases, as a result of Arctic haze; and (iii) daily mean background summer values of $\tau(0.50\ \mu m)$ measured at Tiksi in Siberia were always lower than 0.08 during the summer 2010. With regard to Antarctic aerosol, Tomasi et al. (2007) estimated that the daily mean values of $\tau(0.50\ \mu m)$ were lower than 0.10 during the austral summer months at Marambio, Neumayer, Aboa, Mirny, Molodezhnaya, Syowa, Mario Zucchelli, Kohnen, Dome Concordia and South Pole. In particular, examining the sun-photometer measurements carried out from 2005 to 2010, Tomasi et al. (2012) reported that the austral summer values of $\tau(0.50\ \mu m)$ measured at Neumayer and Mirny were b0.10 during the whole season, while those measured at South Pole never exceeded 0.06.

Therefore, since the values of $\tau(0.44\ \mu m)$ determined from the sun-photometer measurements conducted in polar regions are mostly lower than 0.15 and thus below the value recommended by Gobbi et al. (2007), we have decided not to determine the exponent α_f using the O'Neill et al. (2001b) algorithm, but to calculate the best-fit value of the Ångström exponent α over the spectral range $0.40 \le \lambda \le 0.87\ \mu m$ using Eq. (2). In real cases, the exponent α provides by itself a first rough estimate of the optical influence of the fine particle component on $\tau(\lambda)$, since it gradually decreases on average from cases where fine particle extinction predominates to cases where coarse particles are optically predominant.

In all cases with relatively high values of $\tau(0.50\ \mu m)$, the AERONET and SKYNET sun/sky radiometers can also be used to provide regular measurements of sky-brightness along the solar almucantar (an azimuthal circle around the local normal whose zenith angle equals the solar zenith angle θ_0) and also in the principal plane containing the direction to the Sun and the local normal. The analysis of these measurements enables better constraints for solving the inverse problem (while accounting for multiple scattering and surface reflectance effects) and allowing the following parameters to be derived: (i) the aerosol single scattering albedo $\omega(\lambda)$, (ii) the phase function $P(\Theta)$, (iii) the particle number density size-distribution $N(r) = dN(r)/d(\ln r)$ given as a function of particle radius r, and (iv) the complex refractive index $n(\lambda)$–$i\,k(\lambda)$ (King and Dubovik, 2013).

The data analysis performed in this paper was subject to certain data processing constraints across networks of instruments. In the first instance, all network protocols differ in many (typically) minor details such as the means of estimating molecular optical thicknesses and solar air masses, the nominal time interval between measurements and calibration protocols. In general, all data-sets were cloud-screened using temporal-based criteria that were developed and rigorously tested by each network group. Only Level 2.0 AERONET data were used: this corresponds to temporal-based cloud-screened data (Smirnov et al., 2000) that has undergone a final quality assurance step. The GMD/NOAA data acquired at Barrow and Alert were further cloud-screened using a spectral criterion wherein $\tau(\lambda)$ spectra were eliminated for α b 0.38. This added cloud-screening feature was found to be necessary in order to eliminate the influence of homogeneous, thin cirrus clouds that has escaped the temporal cloud-screening step. Finally we note that the specific spectral ranges of the α computations, while being nominally limited to $0.40 \le \lambda \le 0.87\ \mu m$ are given in Tables 1 and 2 for each type of instrument (the α regression was carried out for all wavelength channels between and including the wavelength extremes given in the "Spectral interval" column).

Before presenting the evaluations of the seasonal variations in parameters $\tau(0.50\ \mu m)$ and α measured at the various Arctic and Antarctic sites, it seems useful for the reader to give a measure of the experimental errors and variability features associated with the aerosol optical characteristics varying as a function of aerosol origin and their chemical composition evolutionary patterns:

(i) the mean experimental error of AOT measured with the most sophisticated sun-photometers leads to an uncertainty of ~0.01 in the visible and near-IR, mainly due to calibration errors (Eck et al., 1999);
(ii) the relative errors of exponent α determined in terms of Ångström's (1964) formula is about twice the relative error of AOT (Gobbi et al., 2007), therefore leading to obtain at polar sites relative errors close to 30% and, hence, absolute errors of ~0.50 (Mazzola et al., 2012); and
(iii) the spread of α arising from the natural variability of Arctic and Antarctic aerosol types has been estimated by Stone (2002), Tomasi et al. (2007) and Treffeisen et al. (2007) to yield average uncertainties of ± 0.4 for Arctic summer background aerosols, ± 0.6 for Arctic aerosols including particular cases (like Asian dust and boreal smoke particles), and ± 0.5 for austral summer background aerosol observed at Antarctic sites.

2.1.1. Measurements in the Arctic

In order to define the seasonal variations in polar aerosol optical characteristics, sun-photometer measurements of $\tau(\lambda)$ conducted at various visible and near-infrared wavelengths can be conveniently examined to evaluate the exponent α in terms of Eq. (2). Such measurements have been carried out at various Arctic and Antarctic sites during the past decades, providing useful information on polar aerosol optical and microphysical features. In fact, $\tau(\lambda)$ gives a measure of the overall aerosol extinction along the vertical atmospheric path, while α depends on the combination of the different extinction effects produced by nuclei, accumulation and coarse particles. Values of α higher than 1.3 are usually observed in air masses where Aitken nuclei and very fine particles (having radii r b ~0.12 μm) optically predominate, while relatively low values of α b 1.0 are observed when accumulation (over the $0.12 \le r \le 1.25\ \mu m$ range) and coarse (over the r N 1.25 μm range) mode particles produce stronger extinction effects. The vertical profile of the aerosol volume backscattering coefficient can be determined by means of lidar measurements, allowing the classification of aerosol layers in the troposphere and lower stratosphere.

Direct solar radiation measurements have been regularly conducted for cloud-free sky conditions at numerous polar sites over the past decades, using multi-spectral sun-photometers of different design. Tables 1 and 2 list the 12 Arctic sites and 9 Antarctic sites, whose data were employed in this study together with their geographical coordinates, measurement periods, the peak wavelengths of the spectral channels used to measure AOT and determine the best-fit value of α, and the main references where the technical characteristics of the instruments are detailed. The geographical locations of these sites are separately indicated in Fig. 2 for the Arctic and Antarctic regions.

The individual measurements of the spectral values of $\tau(\lambda)$ and of the exponent α obtained from the analysis of the field data recorded for cloud-free sky conditions were then averaged to yield daily means. Since the present analysis is devoted to tropospheric aerosols, the sun-photometer measurements conducted in the presence of stratospheric layers of volcanic particles were removed for the following sites and intervals at: (a) the Arctic sites, in May 2006 (Soufrière Hills eruption), October 2006 (Tavurvur eruption) (Stone et al., 2014), from mid-August to late September 2008 (Kasatochi eruption) (Hoffmann et al., 2010), from early July to early October 2009 (Sarychev eruption) (O'Neill et al., 2012), and in April 2010 (Eyjafjallajokull eruption), as well as the sun-photometer data collected at Barrow during the periods that followed both the Okmok eruption in July 2008, and the Mt. Redoubt eruption in March 2009 (Tomasi et al., 2012); and (b) the Antarctic sites, for all data affected by volcanic features comparable to those of Mt. Pinatubo observed from late spring 1992 to late autumn 1994 (Stone et al., 1993; Stone, 2002). Actually, the Stratospheric Aerosol and Gas Experiment (SAGE II) observations made since 2000 over Antarctica did not provide evidence of appreciable extinction features produced by volcanic particle layers at stratospheric altitudes (Thomason and Peter, 2006; Thomason et al., 2008), as also confirmed by the analysis of sun-photometer measurements conducted at Mirny, Neumayer, Mario Zucchelli and South Pole from 2000 to 2010 (Tomasi et al., 2012).

The remaining daily mean "tropospheric" data collected at each site were then subdivided into monthly sub-sets consisting of data measured in different years, for which the multi-year monthly mean values of $\tau(0.50\ \mu m)$ and α were determined. Relative frequency histograms (hereinafter referred to as RFHs) were defined separately using the daily mean values of $\tau(0.50\ \mu m)$ and α collected at Arctic sites during the following seasons: (i) winter–spring, from December to May, when Arctic haze events were most frequent, and (ii) the summer–autumn, from June to October, to characterise background aerosols in summer. For the Antarctic sites, RFHs were determined for austral summer (from late November to February), to define the mean optical characteristics of background aerosols.

2.1.1.1. Measurements in Northern Alaska. Two multi-year sets of sun-photometer measurements from Barrow, located on the Arctic Ocean coast, were analysed in the present study: (a) the first series, acquired with the Carter Scott sun-photometer, was conducted from March 2000 to September 2012 by GMD/NOAA (see Table 1) and consisted of spectral $\tau(\lambda)$ measurements, taken every minute on apparently cloud-free days and then cloud-screened by applying the GMD/NOAA selection procedure (for α(0.412 μm/0.675 μm) b 0.38); and (b) the second series was AERONET data collected from March 2002 to September 2013 (see Table 1). The results are shown in Fig. 3 for the GMD/NOAA and AERONET measurements, where the data coverage is 94% and 78% of the overall 14-year period (March 2000 to September 2013), respectively. The GMD/NOAA monthly mean values of $\tau(0.50\ \mu m)$ increase from about 0.07 in February to more than 0.12 in April and May, and then gradually decrease to less than 0.10 in June and July, and to around 0.05 in October, with (grey toned) standard deviations σ_τ N 0.05 from April to July, and b~0.03 in the other months. Similar results were obtained for the AERONET measurements, which exhibited monthly mean values of $\tau(0.50\ \mu m)$ that increased from about 0.12 in March to more than 0.16 in April, and then decreased to 0.10 in June and August and 0.05 in September and October, with σ_τ N 0.05 from April to August, and b~0.03 for the other months. The monthly mean values of α determined from the GMD/NOAA and AERONET measurements were rather stable from February to April, varying from 1.10 to 1.20, with a standard deviation $\sigma_\alpha = 0.3$ on average, followed by a convex cap from April to August, with values close to 1.50 from May to July, and increasing values from 1.30 to ~1.50 in August–October. Fig. 3 also shows the RFHs of the daily mean values of $\tau(0.50\ \mu m)$ and α measured during the winter–spring and summer–autumn seasonal periods. The analytical curves drawn to represent the RFHs are normal curves and are normalised to yield unit (100%) integration over the measured sampling intervals of

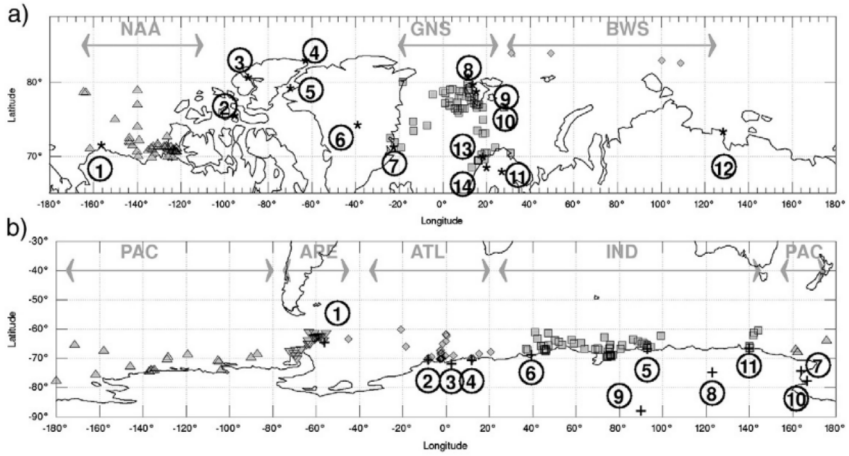

Fig. 2. Part (a): Map of the Arctic with the geographical positions of the ground-based sun-photometer stations (solid stars), labelled with the following numbered circles: (1) Barrow, (2) Resolute Bay, (3) Eureka-0PAL, (4) Alert, (5) Thule, (6) Summit, (7) Ittoqqortoormiit, (8) Ny-Ålesund, (9) Barentsburg, (10) Hornsund, (11) Sodankylä, (12) Tiksi, (13) Andenes/ALOMAR, and (14) Kiruna. Grey symbols indicate the geographical positions of ship-borne sun-photometer measurements made on clear-sky days during the AERONET/MAN cruises in three different sectors: (i) Northern Greenland–Norwegian Sea (GNS), between 20° W and 30° E (squares), (ii) Barents Sea and West Siberian Sea (BWS), between 30° E and 130° E (diamonds), and (iii) Eastern Chuckci Sea, Beaufort Sea and Amundsen Gulf (NAA), between 170° W and 110° W (triangles). Part (b): as in the upper part, for the Antarctic ground-based sun-photometer and/or lidar stations (crosses), labelled with the following numbered circles: (1) Marambio, (2) Neumayer, (3) Troll, (4) Novolazarevskaya, (5) Mirny, (6) Syowa, (7) Mario Zucchelli, (8) Dome Concordia, (9) South Pole, (10) McMurdo, and (11) Dumont d'Urville. Grey symbols indicate the geographical positions of the ship-borne sun-photometer measurement days during the AERONET/MAN cruises, subdivided into the four following oceanic sectors: (i) Southern Indian Ocean (IND), between 20° E and 150° E (squares), (ii) Southern Pacific Ocean (PAC), between 150° E and 75° W (upward triangles), (iii) Southern Atlantic Ocean (ATL), between 50° W and 20° E (diamonds), and (iv) Antarctic Peninsula (APE), between 75° and 50° W (downward triangles).

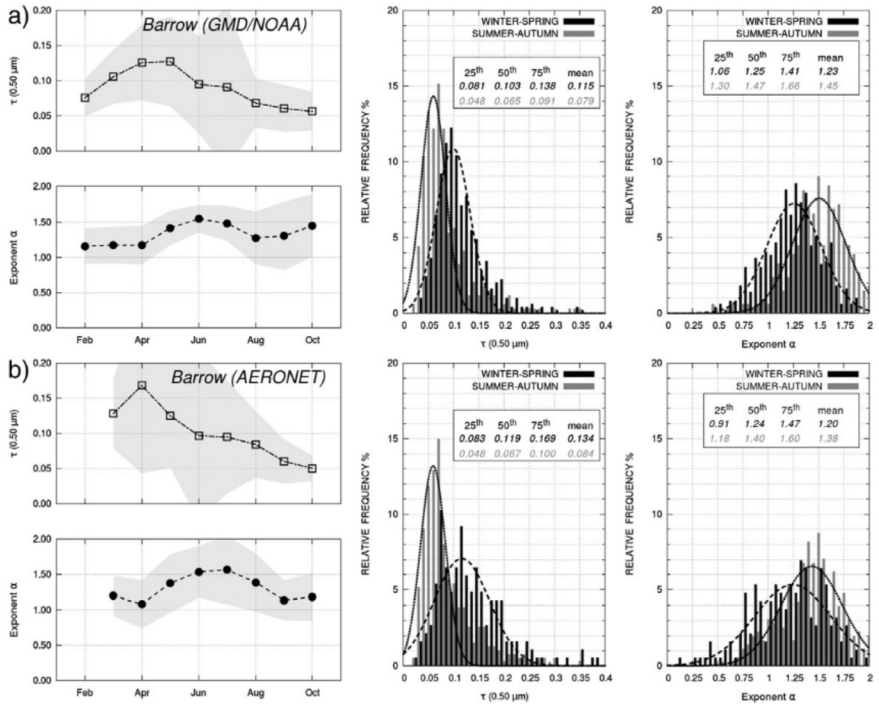

Fig. 3. Left-hand side: Time-patterns of the monthly mean values and standard deviations (defined by the grey shaded areas) of aerosol optical thickness τ(0.50 μm) (open squares) and Ångström wavelength exponent α (solid circles) obtained from both series of multi-year sun-photometer measurements conducted at Barrow (Alaska) by (a) GMD/NOAA (Boulder, Colorado, USA) over the period from March 2000 to September 2012, using the Carter Scott sun-photometers listed in Table 1, and (b) NASA/GSFC (USA) (in cooperation with the Brookhaven National Laboratory (Upton, NY, USA)) over the period from March 2002 to September 2013, using the AERONET Cimel CE-318 sun-photometer having the spectral characteristics given in Table 1. Right-hand side: Relative frequency histograms of τ(0.50 μm) and exponent α obtained separately for the winter–spring (Arctic haze) period from December to May (black colour) and the summer–autumn (background aerosol) period from June to October (grey colour). The seasonal mean values and 25th, 50th, and 75th percentiles of τ(0.50 μm) and α are reported in the boxes inserted into the graphs, as obtained by examining the daily mean values of both optical parameters measured at this coastal site of the Arctic Ocean in the winter–spring (black italics) and summer–autumn (grey italics) periods.

τ(0.50 μm) and α shown in Fig. 3. The RFHs for both instruments were very similar, although showing appreciable discrepancies between the means and percentiles, which are in general lower than the corresponding standard deviations. The seasonal mean values of τ(0.50 μm) were equal to 0.12 and 0.13 in winter–spring, for the GMD/NOAA and AERONET data, respectively, and close to 0.08 in summer–autumn for both data-sets. The RFHs also have long-tails towards high values for winter–spring data, and larger kurtosis in summer–autumn. The long-tail features could in part be ascribed to larger τ(0.50 μm) values in April and May (ranging from 0.12 to 0.16) attributable to the frequent Arctic haze cases observed in spring but would also be, in part, due to the (asymmetrical) log-normal distribution that is arguably a better fit to the AOT RFHs in general (c.f. O'Neill et al., 2000).

The small discrepancies found between the time-patterns of the monthly mean values of τ(0.50 μm) and α defined for both data-sets as well as those between the RFHs of both parameters might well be attributable to slight differences in the total observation periods of both sun-photometers and/or differences in GMD/NOAA and AERONET cloud screening. The different seasonal features of τ(0.50 μm) and α shown in Fig. 3 arise mainly from the origins of the aerosol load, associated with the transport of continental polluted air masses mainly from North America and Asia, in winter–spring (Hirdman et al., 2010). It can also be seen in Fig. 3 that the left-hand wings of the RFHs for α contain some values b0.75: these are probably due to an optical predominance of coarse mode sea-salt aerosols and/or local blown dust. Similarly, a fraction of values with αb 1.20 are presumably related to Asian dust transport episodes (Di Pierro et al., 2011) that are most frequently observed in March and April, and which are generally characterised by persistent extinction features typical of coarse mineral dust particles (Stone et al., 2007).

2.1.1.2. Measurements in Northern Canada (Nunavut). The results derived from the AERONET/AEROCAN measurements conducted at Resolute Bay and Eureka-0PAL, and those carried out by GMD/NOAA at Alert (Canada) (see Table 1) over the past decade are shown in Fig. 4, as obtained for air masses containing aerosols mainly transported from the North American and Arctic Ocean areas (Hirdman et al., 2010) over these three Canadian sites. The monthly mean values of τ(0.50 μm) exhibit: (i) rather high values related to Arctic haze in March–April, varying between 0.10 and 0.15, and (ii) relatively low values in the subsequent months, decreasing to around 0.05 in September at all the three sites. The month-to-month differences, varying on average from 0.05 at Resolute Bay and Alert in March–June to 0.01 at Alert in September, are similar to or smaller than the monthly mean values of σ_τ. The winter–spring RFHs exhibit higher mean values of τ(0.50 μm), ranging from 0.09 to 0.12, and broader right-hand wings compared to the summer–autumn period, where the RFHs are narrower, giving seasonal mean values varying from 0.06 to no more than 0.08.

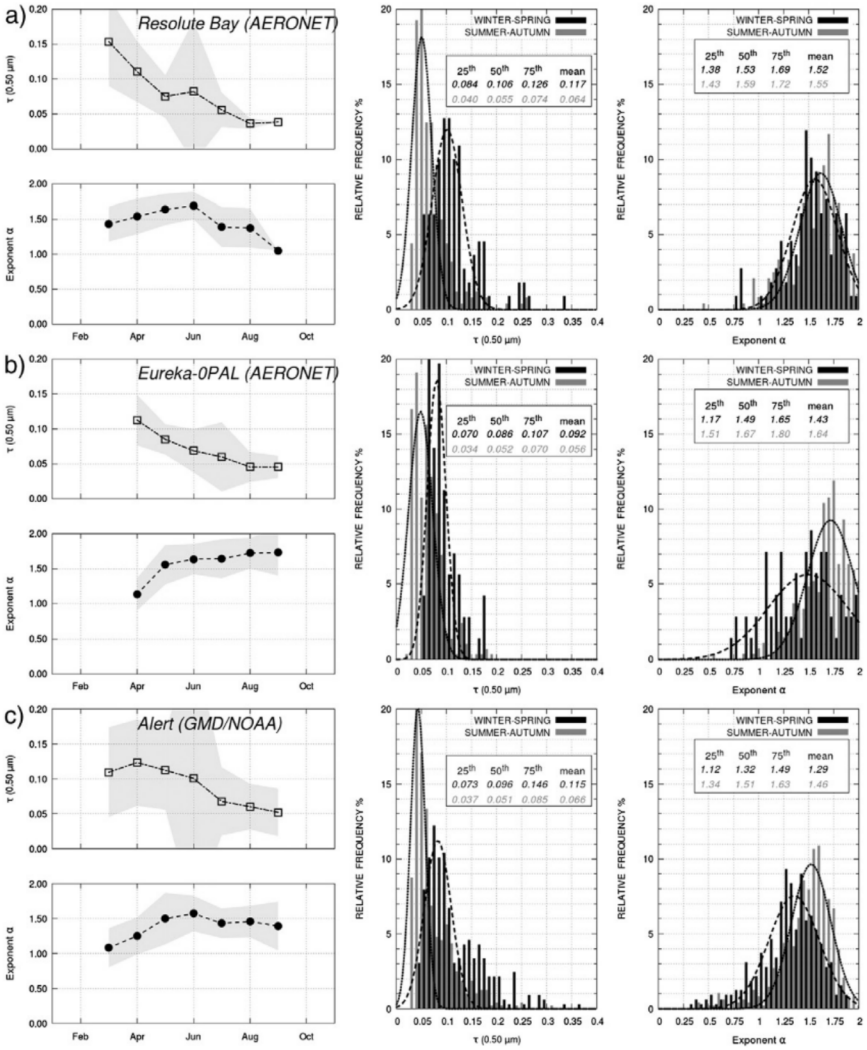

Fig. 4. As in Fig. 3, for the multi-year sun-photometer measurements of aerosol optical thickness τ(0.50 μm) and exponent α conducted at: (a) Resolute Bay by Environment Canada (Ontario, Canada) over the period from July 2004 to October 2012, using the AERONET/AEROCAN Cimel CE-318 sun-photometer having the spectral characteristics given in Table 1; (b) Eureka-0PAL by CARTEL (Sherbrooke University, Canada) from April 2007 to September 2011, using the AERONET/AEROCAN Cimel CE-318 sun-photometer having the spectral characteristics given in Table 1; and (c) Alert by GMD/NOAA (Boulder, Colorado, USA) from August 2004 to September 2012, using the Carter Scott SP02 sun-photometer, with the characteristics given in Table 1.

Relatively small differences were found between the monthly mean values of α in winter–spring and summer–autumn, with: (i) stable values close to 1.50 in March–June at Resolute Bay, gradually decreasing to 1.0 in July–September; and (ii) values increasing from 1.0 to 1.5 in March–June at Eureka and Alert, and remaining close to 1.50 from July to September (with σ_α b ~0.3). The monthly mean values of α determined at Resolute Bay and Eureka-0PAL are appreciably higher than those measured at Barrow, presumably as a result of the weaker extinction produced by coarse sea-salt particles and/or local dust, and weaker contributions of Asian dust in the spring months. Fig. 4 shows that the seasonal RFHs of daily mean α values do not exhibit symmetrical shapes: (i) the winter–spring RFHs are rather wide, showing long-tailed left-hand wings and mean values varying from 1.29 (at Alert) to 1.52 (at Resolute Bay), and (ii) the summer–autumn RFHs are characterised by mean values varying from 1.46 (Alert) to 1.64 (Eureka). Only moderate, relative increases in the coarse particle content occurred at Resolute Bay from winter–spring to summer, while greater winter–spring to summer–autumn variations were measured at Eureka and Alert presumably due to fine particle smoke transported from North American boreal forest fires (Stohl et al., 2006). Finally, it is worth noting that a few cases were found with α b 0.40 at Alert, despite the α b 0.38 cloud-screening rejection criterion. They were

presumably associated with prevailing extinction by coarse mode sea-salt aerosols transported from the Arctic Ocean, especially in the spring months.

2.1.1.3. Measurements in Greenland. Fig. 5 shows the results derived from the multi-year sets of sun-photometer measurements conducted at: (i) the Thule AERONET site, in the north-western corner of Greenland; (ii) the Summit PMOD/WRC site, located in the middle of the Central Greenland ice sheet; and (iii) Ittoqqortoormiit AERONET site, on the eastern coast of Greenland (see Table 1 for details on these sites).

The monthly mean $\tau(0.50\ \mu m)$ values at Thule decreased slowly from about 0.10 in April–May to around 0.05 in June–September, with $\sigma_\tau \sim 0.03$, while α was rather stable with monthly mean values ranging from 1.40 to 1.50 from March to September, with $\sigma_\alpha \sim 0.3$. The winter–spring $\tau(0.50\ \mu m)$ RFH is characterised by a mean value of 0.093 and an asymmetric shape whose long-tailed, right-hand wing is influenced by the frequent occurrences of Arctic haze episodes. The summer–autumn RFH for $\tau(0.50\ \mu m)$ was more symmetric, with mean and median values equal to 0.058 and 0.049, respectively, and values of the 25th and 75th percentiles relatively close to the median value, as can be seen in

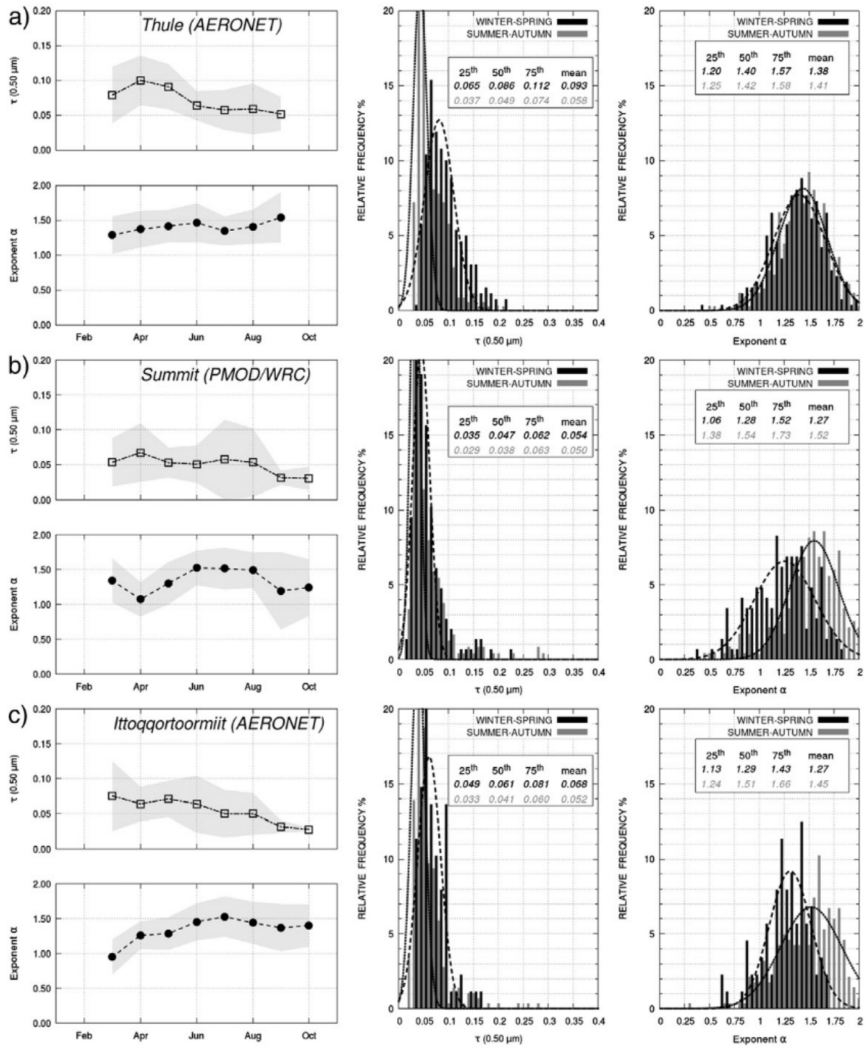

Fig. 5. As in Fig. 3, for the for the multi-year sun-photometer measurements of aerosol optical thickness $\tau(0.50\ \mu m)$ and exponent α conducted at: (a) Thule (North-western Greenland) by NASA/GSFC (USA) over the period from March 2007 to September 2012, using an AERONET Cimel CE-318 sun-photometer having the spectral characteristics reported in Table 1; (b) Summit (Central Greenland) by PMOD/WRC (Switzerland) from January 2001 to October 2011, using a PFR (No. N34) sun-photometer of the GAW-PFR network, having the spectral characteristics given in Table 1; and (c) Ittoqqortoormiit (Eastern Greenland) by NASA/GSFC (USA) over the period from May 2010 to October 2013, using an AERONET Cimel CE-318 sun-photometer having the spectral characteristics reported in Table 1.

Fig. 5. Very similar shapes of both seasonal RFHs for α were obtained, with mean values of 1.38 in winter–spring and 1.41 in summer–autumn, and similar values of the main percentiles from winter–spring to summer–autumn, indicating no relevant seasonal changes in the aerosol size-distribution.

Rather stable monthly mean values of $\tau(0.50\ \mu m)$ were obtained at the high-altitude Summit station, equal to 0.05 ± 0.03 from March to August, and about 0.03 ± 0.01 in September and October. Both seasonal RFHs of the daily mean $\tau(0.50\ \mu m)$ values assumed very similar shapes, with mean values close to 0.05, and values of the main percentiles differing by no more than 0.01 from season to the other. Greater differences were determined between the two seasonal RFHs of α, with mean values equal to 1.27 in winter–spring and 1.52 in summer–autumn, and the main percentiles differing by no more than 0.3. These aerosol optical characteristics indicate that Summit is representative of the Arctic free troposphere, influenced mainly by particulate transport from North America and Europe, and only weakly by Siberian aerosols (Hirdman et al., 2010).

The monthly mean values of $\tau(0.50\ \mu m)$ at Ittoqqortoormiit showed similar seasonal variations to those at Thule, gradually decreasing from ~0.08 in March to less than 0.04 in September–October, with $\sigma_\tau = 0.05$ in spring, gradually decreasing in summer until reaching values of ~0.01 in autumn. The monthly mean α values increase from ~1.00 in March to ~1.50 in summer, and slowly decrease in September and October, varying around 1.40, with $\sigma_\alpha = 0.2$ in March and close to 0.3 in the other months. The RFHs for $\tau(0.50\ \mu m)$ did not vary largely from winter–spring to summer–autumn. The seasonal mean values were equal to 0.068 in winter–spring and 0.052 in summer–autumn, which were not considerably different from the median values in both seasons. They give a measure of the appreciable decrease in $\tau(0.50\ \mu m)$ observed from winter–spring to summer–autumn. The seasonal RFHs for α are more similar to those obtained at Summit than those of Thule. In fact, the winter–spring mean value of α was equal to 1.28, and the summer–autumn value was equal to 1.45. These results suggest that the atmospheric content of fine mode particles increases considerably from winter to summer at Ittoqqortoormiit. Such variations are probably associated with the marked extinction effects produced by maritime accumulation/coarse mode particles in winter–spring and the predominant aerosol extinction effects produced by background continental particles mainly transported in summer–autumn from Europe and North America and containing in general significant loads of both anthropogenic and BFF particles.

The seasonal changes shown in Fig. 5 at the three Greenland sites can be mainly attributed to the variations in aerosol transport processes from anthropogenic/polluted regions or remote oceanic mid-latitude areas, and only rarely to Asian dust. Actually, the transport processes of anthropogenic soot aerosols are known to appreciably enhance $\tau(\lambda)$, yielding rather high values of α in general (Tomasi et al., 2007; Stone et al., 2008). This may also occur in free-tropospheric layers, as observed during airborne measurements conducted at mid-altitudes over the Arctic Ocean (Stone et al., 2010).

2.1.1.4. Measurements in Spitsbergen (Svalbard). The results obtained at Ny-Ålesund, Barentsburg and Hornsund (Svalbard, Norway) from four different series of measurements are shown in Fig. 6, as conducted by AWI (Bremerhaven, Germany) and NILU (Kjeller, Norway) at Ny-Ålesund, IAO-SB-RAS (Tomsk, Russia) at Barentsburg, and the Institute of Geophysics (Warsaw University, PAS, Poland) in cooperation with NASA/GSFC (USA) at Hornsund (see Table 1).

The AWI monthly mean values of $\tau(0.50\ \mu m)$ varied from 0.07 to 0.09 in winter–spring, and considerably decreased in summer–autumn from about 0.05 in June to 0.02 in October, with $\sigma_\tau = 0.03$ on average. The NILU monthly mean values of $\tau(0.50\ \mu m)$ were equal to ~0.10 from March to May, and varied from 0.06 in June–July to less than 0.05 in August–September, with σ_τ equal to 0.04 in spring and 0.03 in summer and autumn. The comparison between the AWI and NILU results shows good agreement, although the NILU values were occasionally higher than those for AWI by no more than 10% on average in spring, such discrepancies probably arising from the slightly dissimilar measurement periods of 14 and 8 years, respectively. The AWI monthly mean values of α increased from less than 1.30 in March to 1.50 in May, and slowly decreased in summer–autumn until reaching a value b1.20 in September and becoming nearly equal to 1.50 in October, with $\sigma_\alpha = 0.30$ on average, while the NILU values increased slowly from 1.20 in March to 1.50 in June, and slowly decreased to ~1.30 in September, with $\sigma_\alpha = 0.20$ in all months. These discrepancies of no more than 15% are in general smaller than the monthly values of σ_α. Therefore, it is not surprising that the RFHs found for the daily mean $\tau(0.50\ \mu m)$ values derived from the AWI and NILU data-sets differ considerably from one season to another: (i) the AWI and NILU winter–spring mean values were equal to 0.082 and 0.089, respectively, with the main percentiles differing by no more than 0.007; and (ii) the AWI and NILU summer–autumn mean values of $\tau(0.50\ \mu m)$ were equal to 0.052 and 0.059, respectively, with $\sigma_\tau = 0.04$ on average, and having differences between the main percentiles no greater than 0.02. The AWI seasonal RFHs of α yielded mean values of 1.32 in winter–spring and 1.28 in summer–autumn, while NILU RFHs gave mean values of 1.35 in winter–spring and 1.38 in summer–autumn. Comparable values of the three main percentiles of the AWI and NILU RFHs were also obtained, differing by less than 0.1 in winter–spring and less than 0.2 in summer–autumn. Therefore, the analysis of the AWI and NILU RFHs of α showed: (i) more dispersed features of α in winter–spring, presumably due to the larger variability of fine and coarse particle concentrations during the frequent Arctic haze episodes, and (ii) values of α mainly varying from 1.00 to 1.60 in summer–autumn, due to the large variability of the fine particle mode atmospheric content (mainly related to BFFs smoke particle transport) with respect to that of accumulation/coarse mode particles (mainly of oceanic origin).

The data-sets of $\tau(0.50\ \mu m)$ and α derived from the Barentsburg IAO measurements consisted of a number of daily measurements smaller than 10% of that given by the AWI and NILU Ny-Ålesund measurements. The monthly mean $\tau(0.50\ \mu m)$ values varied from 0.07 to 0.10, with $\sigma_\tau = 0.02$ on average, and those of α increased from ~0.90 to 1.40 during summer, with $\sigma_\alpha = 0.2$. Therefore, these measurements differ only slightly from those measured at Ny-Ålesund over longer multi-year periods. The RFHs of the daily mean values of $\tau(0.50\ \mu m)$ and α were prepared only for the summer–autumn period, and were found to have a seasonal mean value of $\tau(0.50\ \mu m) = 0.078$, with the main percentiles differing by less than 0.02 from the mean. These values are appreciably higher than those determined at Ny-Ålesund from the AWI and NILU data-sets. A summer–autumn mean value of $\alpha = 1.29$ was obtained, with only slightly differing values of the main percentiles, and a considerably narrower RFH curve than those from the AWI and NILU data-sets measured at Ny-Ålesund.

The Ny-Ålesund results can also be compared in Fig. 6 with the AERONET measurements recorded at Hornsund. The Hornsund results are in close agreement with those of Ny-Ålesund, since the Hornsund monthly mean values of $\tau(0.50\ \mu m)$ varied from 0.10 to no more than 0.12 in winter–spring, with $\sigma_\tau = 0.04$ on average, and from 0.06 to 0.08 in summer–autumn, with σ_τ b 0.03. The monthly mean values of α were rather stable at Hornsund, mainly ranging from 1.20 to 1.50, and showing small differences with respect to the AWI and NILU results. The Hornsund RFHs of $\tau(0.50\ \mu m)$ show that the winter–spring daily mean values were on average higher than those obtained in summer–autumn, by more than 0.03, with differences between the main seasonal percentiles no higher than 0.04. Small variations in α b 0.07 were observed from one season to the other between the seasonal mean values and the main percentiles. The long-tailed left-hand wings of the RFHs of α determined during both seasons suggest that important extinction effects were presumably produced by the sea-salt accumulation/coarse mode particles during both seasons.

The seasonal variations in $\tau(0.50\ \mu m)$ shown in Fig. 6 are mainly due to the different aerosol extinction features produced over the Svalbard region by Arctic haze, especially in spring, and by background aerosol in summer. They are in part associated with the significant seasonal mean decrease in the mean concentration of sulphate particles measured within the atmospheric ground-layer. For instance, on the basis of long-range routine measurements of particulate chemical composition conducted at the Zeppelin station (78° 58′ N, 11° 53′ E, 474 m a.m.s.l.), near Ny-Ålesund (Svalbard), Ström et al. (2003) estimated that the mean mass concentration of nss sulphate ions decreases on average with season, changing from about 3×10^{-1} μg m^{-3} in March–April (for frequent Arctic haze episodes) to around 5×10^{-2} μg m^{-3} in late summer (for background aerosol conditions). These features arise from the fact that the frequent Arctic haze episodes observed in winter and spring over the Svalbard region are mainly due to aerosol transport from the Eurasian area, rather than from North America or East Asia (Hirdman et al., 2010). The region north of 70° N is isolated in summer from the mid-latitude aerosol sources, as demonstrated by Stohl et al. (2006), who analysed aerosol transport patterns into the Arctic. BFF smoke particles are episodically transported over the Svalbard region in summer, from the Siberian region and sometimes from North America (Tomasi et al., 2007; Stone et al., 2008). For instance, huge emissions from BFFs in North America reached Svalbard (Stohl et al., 2006) in July 2004, while agricultural fires in Eastern Europe caused very strong pollution levels in the Arctic during spring 2006 (Stohl et al., 2006; Lund Myhre et al., 2007).

2.1.1.5. Measurements in Scandinavian and Siberian regions. Fig. 7 shows the time-patterns of the monthly mean values of $\tau(0.50\ \mu m)$ and α and the winter–spring and summer–autumn RFHs of both parameters, derived from the sets of FMI/PFR and AERONET sun-photometer measurements carried out at Sodankylä (Northern Finland), and the set of AERONET measurements conducted at Tiksi in Northern-Central Siberia (Russia) (see Table 1).

The FMI/PFR monthly mean values of $\tau(0.50\ \mu m)$ slowly increased from ~0.05 in February to 0.08 in May, remained quite stable from June to August, then slowly decreased to 0.05 in September–October, with comparable values of σ_τ ranging mainly from 0.04 to ± 0.06, without showing clear variations from winter–spring to summer–autumn. The monthly mean values of α increased from about 1.10 in February to over 1.50 in July, and then gradually decreased to 0.75 in November. Different time-patterns of the monthly mean values of $\tau(0.50\ \mu m)$ and α were obtained from the AERONET measurements conducted at Sodankylä over a shorter 7-year period, including only about a third of the daily PFR observations, and giving monthly mean values of $\tau(0.50\ \mu m)$ varying from 0.05 to 0.09 in winter–spring, and from 0.06 to 0.11 in summer, which then decreased to less than 0.04 in September–October. The monthly mean values of α varied from 1.20 to 1.40 in winter–spring, increasing to more than 1.70 in July and decreasing to nearly 1.00 in October.

To provide a more complete picture of the atmospheric turbidity features over Northern Scandinavia, the time-patterns of the PFR and AERONET monthly mean values of $\tau(0.50\ \mu m)$ and α obtained at Sodankylä are compared in Fig. 7 with those determined by Toledano et al. (2012) analysing the $\tau(0.50\ \mu m)$ and α data-sets collected at: (i) Kiruna (67° 51′ N, 20° 13′ E, 580 m a.m.s.l.) in Northern Sweden (270 km WNW from Sodankylä) using the GAW-PFR sun-photometer of the Swedish Meteorological and Hydrological Institute (SMHI) from 2007 to 2010 by, and (ii) Andenes/ALOMAR (69° 18′ N, 16° 01′ E, 380 m a.m.s.l.) in Northern Norway, using the AERONET/RIMA Cimel CE-318 sun-photometer from 2002 to 2007. The Kiruna PFR results are compared in Fig. 7 with those recorded at Sodankylä. The Kiruna monthly mean values of $\tau(0.50\ \mu m)$ were rather stable over the whole measurement period, with σ_τ varying from 0.01 to 0.04, while the monthly mean values of α increased from 1.10 in February to nearly 1.60 in July, and then decreased gradually to ~1.00 in August and 1.20 in October, with values of σ_α varying from 0.10 to 0.25. Thus, the Kiruna monthly mean values of $\tau(0.50\ \mu m)$ closely agree with those measured at Sodankylä and only exhibit small differences between the August–October monthly mean values of α.

A similar comparison is also made in Fig. 7 between the AERONET/FMI results obtained at Sodankylä and the ALOMAR results derived from the AERONET/RIMA Cimel CE-318 sun-photometer measurements at Andenes, from 2002 to 2007. The ALOMAR monthly mean values of $\tau(0.50\ \mu m)$ increased from about 0.04 in February to 0.13 in May, and then slowly decreased to around 0.11 in September–October, having values of σ_τ mainly varying from 0.04 to 0.06. Therefore, the ALOMAR evaluations of $\tau(0.50\ \mu m)$ were in general considerably higher than those measured at Sodankylä, with differences comparable to the standard deviations. The ALOMAR monthly mean values of α varied at Andenes from about 0.85 to 1.05 in February–May, increased in the following months to ~1.30, and subsequently decreased in late summer and autumn to reach a value close to 1.00 in October, with σ_α varying mainly from 0.20 in winter–spring to 0.40 in summer–autumn. These findings indicate that the ALOMAR monthly mean values of α were considerably higher than the AERONET evaluations obtained at Sodankylä, by about 15% on average, presumably because of the more pronounced extinction effects by maritime particles.

The time-patterns of the monthly mean values of $\tau(0.50\ \mu m)$ and α shown in Fig. 7, as obtained by us at Sodankylä, and at Kiruna and Andenes by Toledano et al. (2012) differ appreciably from those typically observed at the other Arctic sites located at higher latitudes and shown in Figs. 3–6. The reason for such differences is that the air masses reaching Northern Scandinavia during the year originate from the Eurasian continent and mid-latitude Atlantic Ocean in 56% of cases, and from the Arctic Basin and Northern Atlantic Ocean in the remaining 44% (Aaltonen et al., 2006). Due to the alternation of polluted air masses from Eurasia with sea-salt particles from ocean areas, the monthly mean values of $\tau(\lambda)$ were rather stable over the entire year, while the monthly mean values of α were higher in early summer, when the Arctic Basin was the principal aerosol source. Because of the efficient transport processes taking place during the year from continental polluted or ocean areas, the FMI/PFR and AERONET Sodankylä RFHs of $\tau(0.50\ \mu m)$ did not exhibit significant differences between the seasonal mean values and the main percentiles defined in winter–spring and summer–autumn. These had monthly mean values of around 0.08 and 0.07 in winter–spring, respectively, with the main percentiles differing by no more than 0.01, and summer–autumn monthly mean values close to 0.07 on average, with differences of about 0.01 between the main percentiles. The FMI/PFR and AERONET Sodankylä monthly mean values of α decreased by 0.10–0.20 on average, from winter–spring to summer–autumn. Clearer discrepancies over both seasonal periods were found, with FMI mean values of about 1.32 and 1.52 in winter–spring and summer–autumn, respectively, and AERONET mean values equal to 1.23 and 1.44 in the same two seasons, providing similar values of the main seasonal percentiles.

A comparison between the winter–spring and summer–autumn estimates of $\tau(0.50\ \mu m)$ and α was not made at Tiksi, since AERONET sun-photometer measurements have been routinely conducted at this remote Siberian site only over the May–October period. The monthly

Fig. 6. As in Fig. 3, for the sun-photometer measurements of aerosol optical thickness $\tau(0.50\ \mu m)$ and exponent α conducted on Spitsbergen Island (Svalbard, Norway) at: (a) Ny-Ålesund by AWI (Bremerhaven, Germany) from April 2000 to September 2013, using the sun- and star-photometers listed in Table 1; (b) Ny-Ålesund by NILU (Kjeller, Norway) from April 2002 to September 2004 and from March 2006 to September 2013, using a PFR (No. N18) sun-photometer of the GAW network; (c) Barentsburg by IAO-SB-RAS (Tomsk, Russia) in the April–August months of 2011 and 2012, using the SPM portable sun-photometer having the characteristics reported in Table 1, and (d) Hornsund by NASA/GSFC (USA) in cooperation with the Warsaw University (PAS, Poland from April 2005 to August 2013), using an AERONET Cimel CE-318 sun-photometer having the characteristics reported in Table 1.

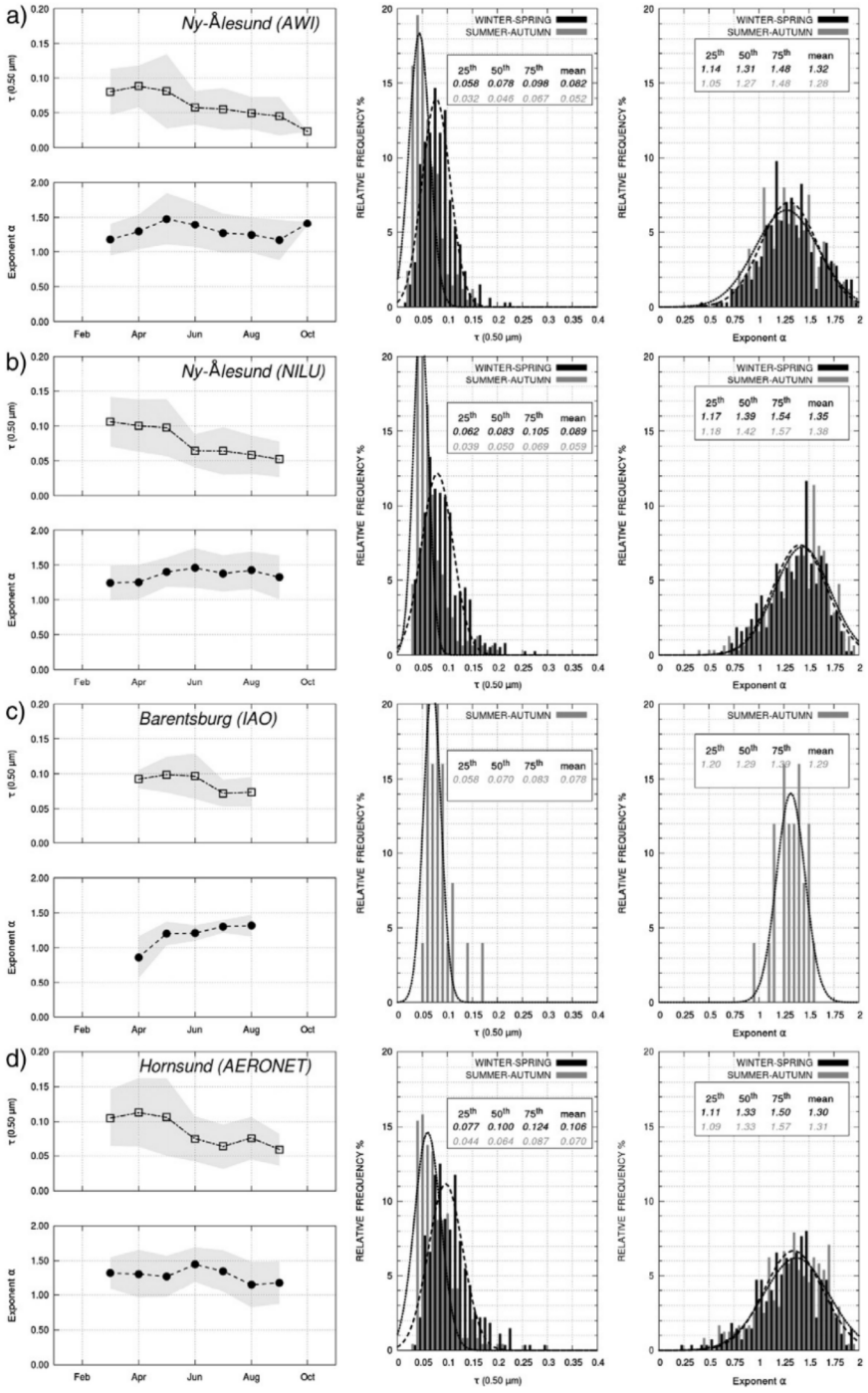
a)
Ny-Ålesund (AWI)
b)
Ny-Ålesund (NILU)
c)
Barentsburg (IAO)
d)
Hornsund (AERONET)
τ (0.50 μm)
Exponent α
Feb
Apr
Jun
Aug
Oct
RELATIVE FREQUENCY %
WINTER-SPRING
SUMMER-AUTUMN
25th 50th 75th mean
0.058 0.078 0.098 0.082
0.032 0.046 0.067 0.052
1.14 1.31 1.48 1.32
1.05 1.27 1.48 1.28
0.062 0.083 0.105 0.089
0.039 0.050 0.069 0.059
1.17 1.39 1.54 1.35
1.18 1.42 1.57 1.38
0.058 0.070 0.083 0.078
1.20 1.29 1.39 1.29
0.077 0.100 0.124 0.106
0.044 0.064 0.087 0.070
1.11 1.33 1.50 1.30
1.09 1.33 1.57 1.31

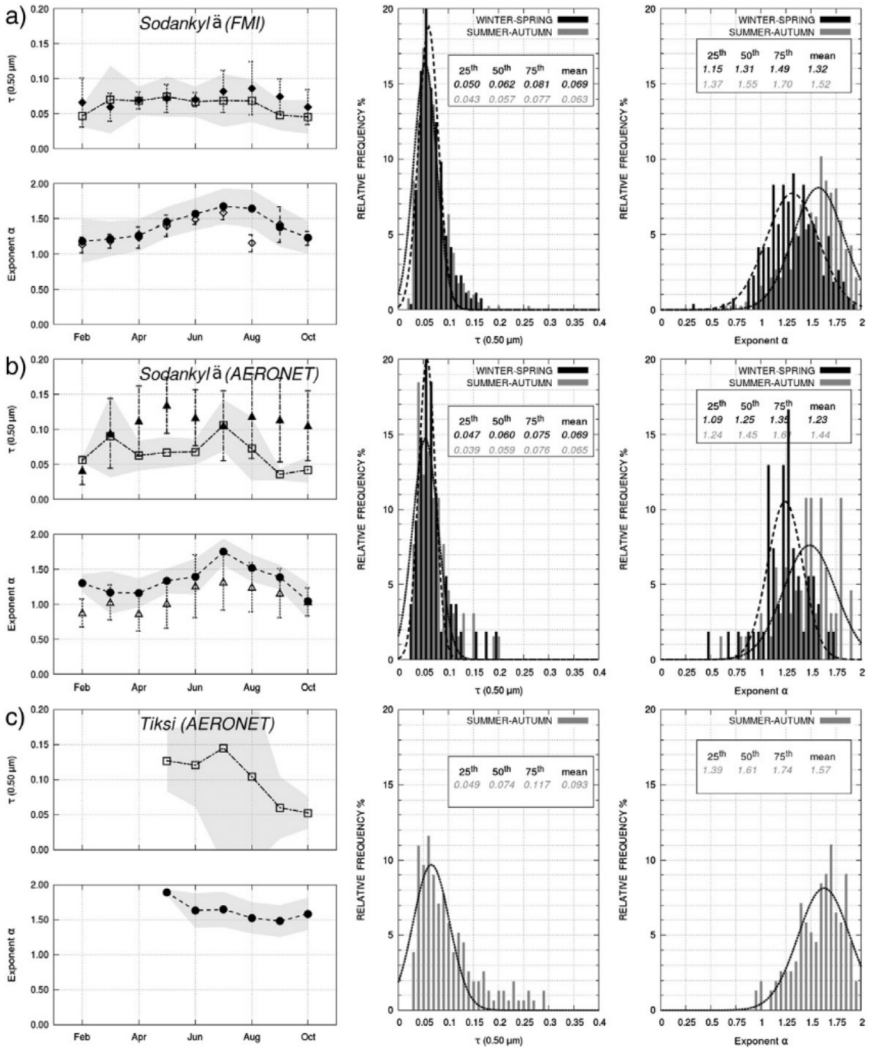

Fig. 7. As in Fig. 3, for the sun-photometer measurements of aerosol optical thickness $\tau(0.50\ \mu m)$ and exponent α conducted at: (a) Sodankylä (Northern Finland) by FMI (Helsinki, Finland) in the winter–spring and summer–autumn periods from late May 2004 to March 2013, using a PFR (No. N32) sun-photometer having the characteristics reported in Table 1, (b) Sodankylä by NASA/GSFC (USA) in cooperation with FMI (Helsinki, Finland) from February 2007 to November 2013, using an AERONET Cimel CE-318 sun-photometer having the characteristics reported in Table 1; and (c) Tiksi (North-central Siberia, Russia) by NASA/GSFC (USA) in the summer–autumn months (June–October) of 2010, 2011 and 2012, using an AERONET Cimel CE-318 sun-photometer having the characteristics given in Table 1. In the first graphs, the time-patterns of the monthly mean values of $\tau(0.50\ \mu m)$ and α (solid and open diamonds, respectively) estimated by Toledano et al. (2012) at Kiruna from PFR measurements conducted over the 2007–2010 period are shown with their standard deviations (vertical bars) for comparison with the FMI results found at Sodankylä. The time-patterns of the monthly mean values of $\tau(0.50\ \mu m)$ and α (solid and open triangles, respectively) estimated by Toledano et al. (2012) at Kiruna from the Cimel CE-318 measurements conducted from 2002 to 2007 are shown in the seconda graph for comparison with those derived from the AERONET measurements carried out at Sodankylä.

mean values of $\tau(0.50\ \mu m)$ exhibit a clear increase from ~0.13 in May to 0.16 in July, with large average values of $\sigma_\tau = 0.14$, followed by a marked decrease in the subsequent months to about 0.05 ± 0.03 in October. Such large variations in $\tau(0.50\ \mu m)$ were associated with a slow decrease in the monthly mean values of α from 1.9 in May to ~1.5 in September, for which $\sigma_\alpha \leq 0.2$. The rather high values of $\tau(0.50\ \mu m)$ and α determined in summer were probably due to the frequent BFF smoke transport episodes from the inner regions of Siberia. In fact, the summer–autumn RFH of $\tau(0.50\ \mu m)$ exhibits a mean value close to 0.09 and a value of the 75th percentile equal to 0.12, which are both appreciably higher than those measured at Sodankylä in summer. The RFH of α yields a mean value of 1.57, and shows a long-tailed left-hand wing with 25th percentile of 1.39, and a long-tailed right-hand wing with 75th percentile of 1.74. This rather high value is

probably associated with small fine particles generated by combustion processes, which dominate extinction effects.

In summary, the Arctic results provide evidence of the seasonality of $\tau(0.50\ \mu m)$ and α. A scatter plot of the median values of α versus those of $\tau(0.50\ \mu m)$ is shown in Fig. 8a, separately for the winter–spring and summer–autumn seasonal periods. Fig. 8a shows that the median values of α vary from 1.10 to 1.70 over the whole year, with: (i) winter–spring median values of $\tau(0.50\ \mu m)$ ranging from 1.20 to 1.50 over the 0.04–0.12 range, and (ii) summer–autumn median $\tau(0.50\ \mu m)$ values all smaller than 0.08 and mainly ranging from 1.30 to 1.70. These features suggest that appreciable differences characterise aerosol extinction in: (a) winter–spring, when the median values of $\tau(0.50\ \mu m)$ vary greatly from one Arctic site to another. This results from their dependency on the importance of particulate transport from the most densely populated mid-latitude regions towards the Arctic, which is particularly strong in late winter and early spring; and (b) summer, when the background aerosol composition varies from one site to another, as a result of different extinction characteristics of fine and coarse mode particles transported from remote regions.

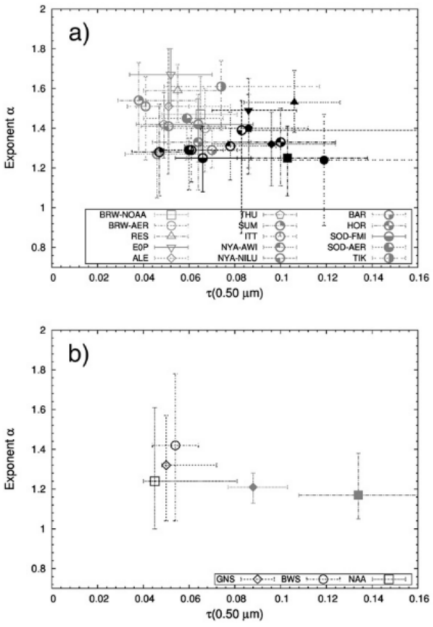

Fig. 8. Upper part (a): Scatter plot of the seasonal median values of the Ångström exponent α versus the corresponding seasonal median values of aerosol optical thickness $\tau(0.50\ \mu m)$ determined from the sun-photometer measurements listed in Table 1. Acronym key: Barrow (BRW-NOAA for the GMD/NOAA measurements, and BRW-AER for the NASA/GSFC AERONET measurements), Resolute Bay (RES), Eureka-0PAL (E0P), Alert (ALE) Thule (THU), Summit (SUM), Ittoqqortoormiit (ITT), Ny-Ålesund (NYA-AWI and NYA-NILU, for the AWI and NILU measurements, respectively), Barentsburg (BAR), Hornsund (HOR), Sodankylä (SOD-PFR and SOD-AER, for the PFR and AERONET measurements, respectively) and Tiksi (TIK). The median values are represented using grey-solid and grey-and-white open symbols to represent the summer–autumn results (as shown in the legend) and solid or black-and-white open symbols to represent the winter–spring results, showing the background aerosol and Arctic haze optical characteristics, respectively. The 25th and 75th percentiles are used to define the limits of the vertical and horizontal dashed bars. Part (b), as in the upper part (a), for the winter–spring (grey symbols) and summer–autumn (open symbols) median values of α plotted versus the corresponding median values of $\tau(0.50\ \mu m)$, as obtained from the seasonal sets of ship-borne sun-photometer measurements collected over the Arctic Ocean sectors: (i) GNS (Greenland Sea and Norwegian Sea) (diamonds), (ii) BWS (Barents Sea and West Siberian Sea) (circles), and (iii) NAA (North American Arctic ocean, including the East Chukchi Sea, the Bering Strait, the Beaufort Sea and the Amundsen Gulf) (squares).

2.1.2. Measurements in Antarctica

Ground-based sun-photometer measurements of aerosol optical parameters have been conducted in Antarctica during the short austral summer period. In the present study, nine multi-year sets of measurements made since 2000 have been analysed (see Table 2), collected at six coastal sites (Marambio, Neumayer, Novolazarevskaya, Mirny, Syowa, and Mario Zucchelli), a mid-altitude station (Troll) and two high-altitude sites (Dome Concordia and South Pole).

2.1.2.1. Measurements at coastal and mid-altitude sites. The results obtained from the sun-photometer measurements carried out at Marambio, Neumayer and Troll are presented in Fig. 9. The Marambio measurements were conducted from September to April, and provided monthly mean values of $\tau(0.50\ \mu m)$ varying from ~0.03 in January to 0.06 in March (with σ_τ varying from 0.02 to 0.04) and α ranging from 0.50 in March to 1.50 in November–January (with $\sigma_\alpha = 0.50$ on average). The austral summer RFHs exhibit regular features with mean values of $\tau(0.50\ \mu m) = 0.038$ and $\alpha = 1.20$, probably due to sea-salt particles, which dominate extinction. The Neumayer measurements were conducted over the September–April period, showing rather stable time-patterns of the monthly mean values of $\tau(0.50\ \mu m)$, ranging from 0.04 to 0.06 (with $\sigma_\tau = 0.03$ on average) and associated with very stable values of α varying from 0.50 to 1.00 (with $\sigma_\alpha = 0.3$ on average), which indicate that aerosols are mostly of oceanic origin. The RFHs of both optical parameters are similar to those determined at Marambio, showing mean values of $\tau(0.50\ \mu m) = 0.041$ and $\alpha = 0.82$, confirming that these stable extinction features are mainly produced by sea-salt particles. The time-patterns of the monthly mean values of $\tau(0.50\ \mu m)$ and α measured at Troll, about 235 km from the Atlantic Ocean coast in the Queen Maud Land, were also quite stable from September to April, yielding values of $\tau(0.50\ \mu m)$ varying from ~0.02 to 0.03 (with σ_τ b 0.005), and values of α slowly increasing from 1.25 in September to ~1.50 in January, and then decreasing to 1.00 in April. The RFH of $\tau(0.50\ \mu m)$ exhibits nearly symmetrical features with little dispersion, with a mean value of 0.023, and 25th and 75th percentiles equal to 0.019 and 0.026, respectively, while the RFH of α was also quite symmetrical over the 0.60–2.10 range, with a mean value of 1.42 and 25th and 75th percentiles differing by less than 0.4 one from the other. These estimates of $\tau(0.50\ \mu m)$ and α differ appreciably from those obtained at Marambio and Neumayer, showing that the aerosol extinction features are only in part produced by maritime aerosols at this mid-altitude site, and in part by fine mode particles, such as nss sulphate aerosols.

Fig. 10 shows the results obtained from the measurements conducted at Novolazarevskaya (Queen Maud Land) and Mirny (on the Davis Sea coast), using various sun-photometer models during different years, as reported in Table 2. The monthly mean values of $\tau(0.50\ \mu m)$ obtained at Novolazarevskaya were very close to 0.02 ± 0.01 over the whole period, while α varied from about 0.80 in November to 1.10 in January, with σ_α equal to 0.10 in the first two months and 0.50 in January and February. The RFH of $\tau(0.50\ \mu m)$ exhibited a leptokurtic curve, with mean value close to 0.02, while a more dispersed distribution curve was shown by the RFH of α, with the mean value close to unity, and 25th and 75th percentiles differing by less than 0.20 from it. The monthly mean values of $\tau(0.50\ \mu m)$ determined at Mirny varied from 0.02 to 0.03 (with $\sigma_\tau = 0.01$), and those of α from 1.50 to 2.00 in September–January, which then slowly decreased to ~1.20 in April. The RFH of $\tau(0.50\ \mu m)$ exhibited features which had a nearly symmetrical peak, with a mean value of 0.025, only slightly differing from that obtained at Novolazarevskaya, while the RFH of α was found to be dispersed and platykurtic, having a mean value of 1.60, and 25th and 75th percentiles differing by more than 0.40 from the mean value. Therefore, it can be concluded that the aerosol extinction features

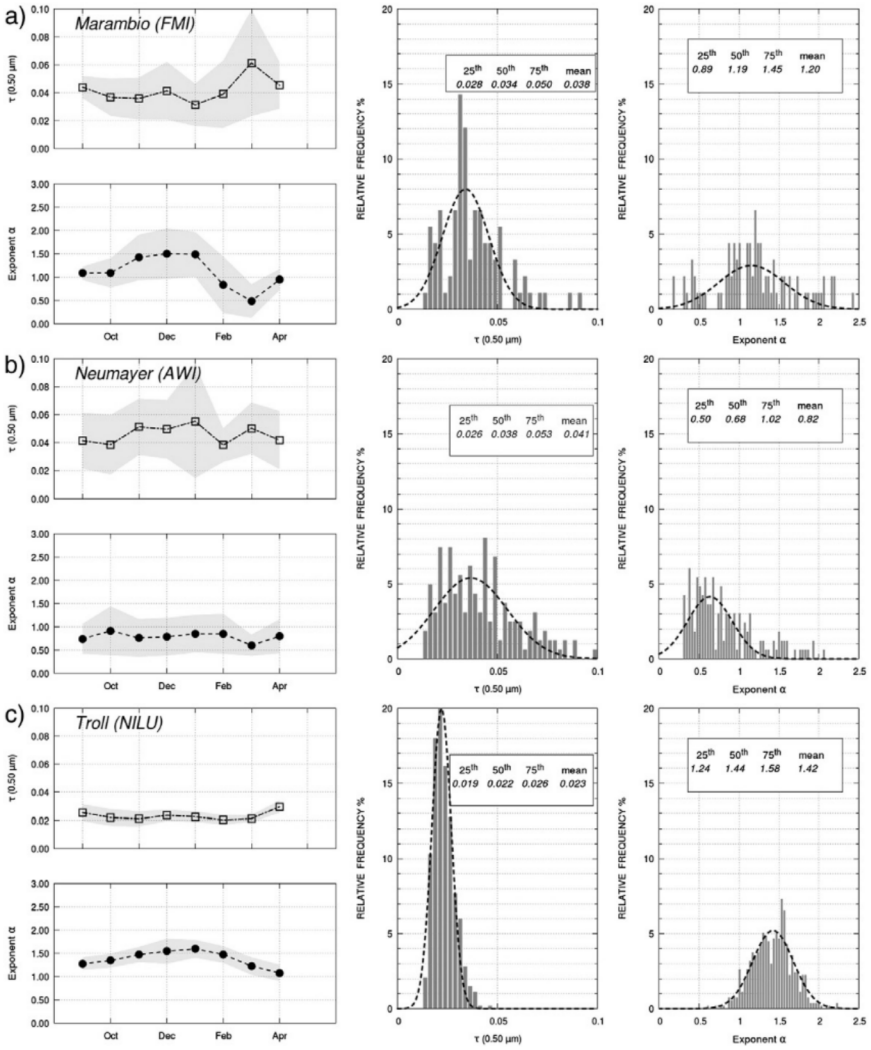

Fig. 9. As in Fig. 3, for sun-photometer measurements of aerosol optical thickness $\tau(0.50\ \mu m)$ and exponent α conducted during the September–April period at: (a) Marambio in the Seymour–Marambio Island (Antarctic Peninsula) by FMI (Helsinki, Finland), using a PFR (No. N29) sun-photometer from August 2011 to March 2013; (b) Neumayer on the Akta Bay (Weddel Sea coast) by AWI (Bremerhaven, Germany), using the sun-photometers SP1A and SP2H, and the star-photometer STAR01 listed in Table 2 from September 2000 to April 2007; and (c) Troll located at Jutulsessen (in the Queen Maud Land, 235 km from the coast, at 1309 m a.m.s.l.) by NILU (Kjeller, Norway), alternately using two PFR (Nos. N40 and N42) sun-photometers from January 2007 to April 2013.

shown in Fig. 10 are predominantly produced by sea-salt particles generated by winds over the ocean, yielding values of α mainly ranging from 0.50 to 1.30.

The results derived from the measurements conducted at Syowa and Mario Zucchelli are shown in Fig. 11, as obtained using various sun-photometer models over the different periods reported in Table 2. The monthly mean values of $\tau(0.50\ \mu m)$ varied from less than 0.02 to ~0.04 over the September–April period (with σ_τ b 0.03), while the monthly mean values of α were also very stable, and described a large maximum of around 1.30 in December, with minima of ~1.00 in September and ~0.90 in April. The RFH of $\tau(0.50\ \mu m)$ assumed a mesokurtic shape, skewed to the right, with the mean value close to 0.02, while the RFH of α exhibited mesokurtic and symmetrical features, arising from sea-salt particles, which caused the predominant extinction. The ISAC-CNR measurements conducted at Mario Zucchelli provided the time-patterns of the monthly mean values of $\tau(0.50\ \mu m)$ shown in Fig. 11, which were close to 0.02 in November and December (with $\sigma_\tau = 0.01$) and then increased to ~0.04 in January and February (with $\sigma_\tau = 0.02$), while the monthly mean values of α were stable and very close to 1.00 from November to January, and equal to ~0.80 in February (with σ_α not exceeding 0.30). The RFHs of $\tau(0.50\ \mu m)$ and α were found to exhibit more dispersed features than those determined at Syowa and

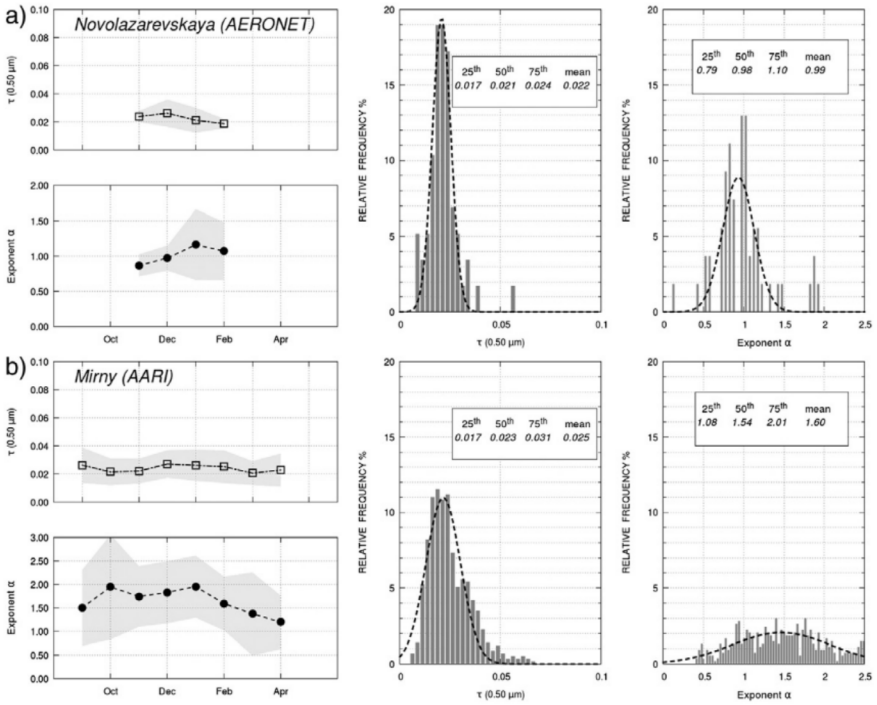

Fig. 10. As in Fig. 3, for sun-photometer measurements of aerosol optical thickness $\tau(0.50\ \mu m)$ and exponent α conducted at the Antarctic sites of: (a) Novolazarevskaya in the Schirmaker Oasis (Quenn Maud Land), 75 km from the coast, by AARI (St. Petersburg, Russia), using a hand-held Microtops calibrated at GSFC (USA) over the periods from December 2008 to February 2009 and from November 2009 to February 2010, and obtaining Level 1.5 cloud-screened data; and (b) Mirny on the Davis Sea coast by AARI (St. Petersburg, Russia), using the AARI, SPM and Microtops sun-photometers, having the spectral characteristics given in Table 2, over the period from March 2000 to October 2013.

both Russian stations, giving mean values equal to 0.04 and 0.96, respectively. However, they clearly indicate that aerosol extinction is mainly due to sea-salt particles at this coastal site, yielding values of α ranging in general from 0.50 to 1.30.

2.1.2.2. Measurements at the high-altitude sites on the Antarctic Plateau. The results obtained analysing the sun-photometer measurements conducted since 2000 at the Dome Concordia and South Pole high-altitude sites are shown in Fig. 12. The measurements were conducted by five groups using different instruments over distinct periods, as reported in Table 2. Due to the background transport of aerosols from very remote sources and the predominant role of subsidence processes on the aerosol load, the time-patterns of the monthly mean values of $\tau(0.50\ \mu m)$ determined at Dome Concordia with different sun-photometers were found to be very stable, mainly ranging from 0.02 to 0.04 (with σ_τ evaluated to be ≤ 0.01) in September–April. The corresponding monthly mean values of α mainly varied from 1.00 to 2.00, with $\sigma_\alpha = 0.20$ on average. The RFH of $\tau(0.50\ \mu m)$ exhibited a well-marked leptokurtic shape, with a mean value close to 0.02, while the RFH of α showed dispersed features over the 0.5–2.2 range, with a mean value close to 1.40, and 25th and 75th percentiles equal to about 1.0 and 1.80, respectively.

The South Pole multi-year measurements conducted by GMD/NOAA at the Amundsen-Scott base were found to provide very stable time–patterns of the monthly mean values of $\tau(0.50\ \mu m)$, mainly ranging from September to March from ~0.02 and 0.04 (with $\sigma_\tau = 0.01$ on average), and monthly mean values of α varying from 1.00 to 2.00, with the highest values in October and November (with $\sigma_\alpha = 0.10$ on average). The AERONET monthly mean values of $\tau(0.50\ \mu m)$ were found to increase from about 0.01 to 0.02 over the November–February period, with $\sigma_\tau = 0.01$ on average, the uncertainty of these measurements being primarily due to both calibration (estimated by Eck et al. (1999) to be of ~0.01 in the visible), and forward scattered light entering the instrument (Sinyuk et al., 2012). Very stable monthly mean values of $\alpha \sim 1.00$ were correspondingly found, with $\sigma_\alpha = 0.50$ on average. Both RFHs of $\tau(0.50\ \mu m)$ derived from the GMD/NOAA and AERONET measurements assumed very narrow and "peaked" curves, with mean values of around 0.02, which appeared to be slightly skewed to the right. The corresponding RFHs of α presented dispersed features over the 0.50–2.00 range, with mean values of 1.54 and 1.06. Although such clearly dispersed results suggest the presence of an important fraction of large-size particles, it is important to take into account that a predominant particulate mass fraction of around 66% was estimated to consist of nss sulphates at South Pole, with lower concentrations of nitrates and sea-salt particles (Arimoto et al., 2004; Tomasi et al. 2012), mainly associated with the background transport of aerosols from very remote sources and the strong effects exerted by subsidence processes. A few cases showing values of α b 0.50 were probably caused by consistent loads of diamond dust ice-crystals within the lower planetary boundary layer (hereinafter referred to as PBL), due to wind mobilisation.

The covariance of the median values of $\tau(0.50\ \mu m)$ and α obtained at the nine Antarctic sun-photometer stations is shown in Fig. 13a. There are two clusters: (i) the first at coastal sites, where the median values of $\tau(0.50\ \mu m)$ were in general considerably higher (at least by a factor two) than those found at the high-altitude Antarctic sites, and the

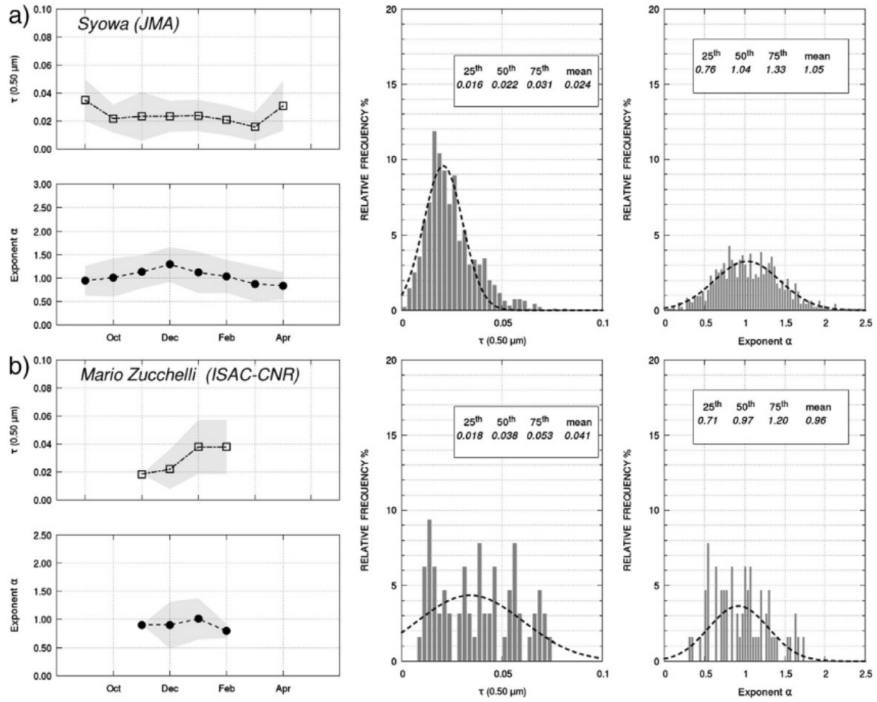

Fig. 11. As in Fig. 3, for sun-photometer measurements of aerosol optical thickness $\tau(0.50\ \mu m)$ and exponent α conducted at the Antarctic sites of: (a) Syowa (East Ongul Island, Lützow-Holm Bay) over the period from January 2000 to December 2011 by the Office of Antarctic Observation (Japan Meteorological Agency, Tokyo, Japan), using the EKO MS-110 sun-photometer, having the spectral characteristics given in Table 2; and (b) Mario Zucchelli on the Terra Nova Bay (Ross Sea, Victoria Land) during the austral summer periods of 2001/2002 and 2005/2006 by ISAC-CNR (Bologna, Italy), using the PREDE POM-01 L and the ASP-15WL sun-photometers, having the spectral characteristics given in Table 2.

median values of α are in general smaller than 1.20, and (ii) the second cluster, with lower median values of $\tau(0.50\ \mu m)$ and median values of $\alpha \geq 1.40$, for which aerosol extinction is predominantly due to sea-salt coarse particles. It is interesting to note that lower median values of $\tau(0.50\ \mu m)$ associated with higher values of α were observed at the coastal sites of Mirny and Marambio, probably because of aeolian fine particles, which dominated extinction effects when compared to sea-salt particles. The median values of $\tau(0.50\ \mu m)$ and α determined at the Troll mid-altitude station indicate that the extinction effects exhibit intermediate features at this non-coastal site. This can probably be attributed in part to sea-salt aerosol and in part to background nss sulphate aerosol transported over large distances, which themselves contribute towards an appreciable enhancement in α. As can be seen in Fig. 13a, the weak median values of $\tau(0.50\ \mu m)$ and relatively strong median values of α at Dome Concordia and South Pole (the latter being partially obscured by the DMC-OPAR symbol) show that atmospheric aerosol extinction is rather weak above the Antarctic Plateau and mainly produced by fine particles consisting of nss sulphates. The lower extremes of the α error bars and the low α value of the AERONET South Pole point are likely due to near-surface diamond dust layers that are observed on windy, cloud-free days at these sites.

3. Ship-borne measurements

A large number of ship-borne measurements of the main columnar aerosol radiative parameters $\tau(\lambda)$ and α were made over the Arctic and Antarctic oceanic regions during the past 10 years. The cruises were conducted by research groups and institutions from different countries, using hand-held Microtops II sun-photometers calibrated at the NASA/GSFC calibration facility. As can be seen in Fig. 2, large areas of the polar oceans were studied during these cruises, yielding an exhaustive picture of aerosol optical characteristics in these high-latitude remote regions. These ship-borne sun-photometer measurements were conducted as a part of the activities promoted and developed in the framework of the Maritime Aerosol Network (MAN), which is a component of the AERONET network (see http://aeronet.gsfc.nasa.gov/new_web/maritime_aerosol_network.html). The measurements of $\tau(\lambda)$ were carried out at visible and near-infrared wavelengths. Arctic Ocean cruises are listed in Table 3, while those taken in the oceanic regions around Antarctica are listed in Table 4. The hand-held Microtops II sun-photometers are equipped with five narrow-band interference filters with peak wavelengths of 0.340 (or 0.380), 0.440, 0.675, 0.870 and 0.936 μm for most cruises, or 0.440, 0.500, 0.675, 0.870 and 0.936 μm in other cruises, as reported in Tables 3 and 4. The first four filters of each spectral set were used to measure the spectral values of $\tau(\lambda)$ and determine the best-fit value of exponent α over the wavelength range from 0.440 to 0.870 μm, while the measurements taken at 0.936 μm were combined with those made within the nearby channel centred at 0.870 μm to evaluate precipitable water (Smirnov et al., 2009). Among the data-sets available at the MAN website, we only selected measurements conducted since 2006 at latitudes higher than 67° N in the Arctic and within ocean areas far by no more than 1000 km from the Antarctic coasts. In addition, the measurement sets obtained by Tomasi et al. (2007) during the RV Oceania cruises made in the summer months of 2003 and 2006 were included in the present analysis.

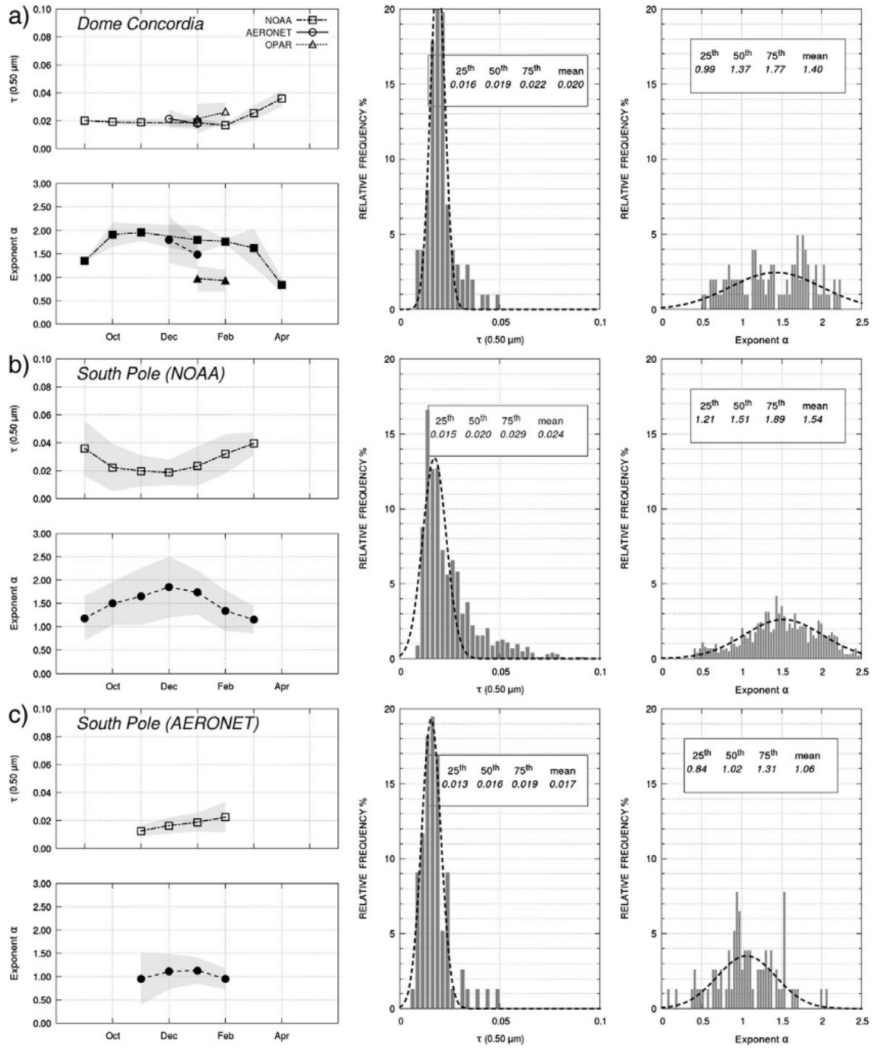

Fig. 12. Upper part: as in Fig. 3, for sun-photometer measurements of aerosol optical thickness τ(0.50 μm) and exponent α conducted at: (a) the high-altitude site of Dome Concordia (DomeC), on the Eastern Antarctic Plateau, over the period from September to April, by (i) GMD/NOAA (Boulder, Colorado, USA) from January to November 2010, using a Carter Scott SP02 sun-photometer (squares); (ii) NASA/GSFC (USA) in cooperation with LGGE/CNRS (Grenoble, France) in January and December of 2003, and in January 2004, using an AERONET Cimel CE-318 sun-photometer having the spectral characteristics reported in Table 2 (circles); and (iii) OPAR Institute (University of Réunion, St. Denis, France) in January of 2010, 2011 and 2012, using an hand-held Microtops II sun-photometer calibrated at GSFC (USA), obtaining Level 1.5 cloud-screened data (triangles). Lower part: as in Fig. 3, for sun-photometer measurements of aerosol optical thickness τ(0.50 μm) and exponent α conducted at the high-altitude site of South Pole (SPO) by (i) GMD/NOAA (Boulder, Colorado, USA), using a Carter Scott SP02 sun-photometer in the September–March period from November 2001 to March 2012; and (ii) NASA/GSFC (USA) in cooperation with GMD/NOAA (Boulder, Colorado, USA) using an AERONET Cimel CE-318 sun-photometer having the spectral characteristics reported in Table 2 in the November–February period from November 2007 to December 2012.

3.1. Aerosol measurements in the Arctic Ocean

Fourteen Arctic Ocean cruises were selected for this study, as summarised in Table 3. The data-set collected during the cruise of RV Polarstern (Alfred Wegener Institute (AWI), Bremerhaven, Germany) in August–September 2009 was not examined to evaluate the background tropospheric aerosol extinction features, because these measurements were found to be strongly affected by the extinction of stratospheric volcanic aerosols generated by the Sarychev eruption in July–October 2009. No evidence of Sarychev volcanic particle extinction at stratospheric levels was found in CALIPSO (Cloud-Aerosol Lidar and Infrared Pathfinder Satellite Observations) data recorded over the Beaufort Sea (O'Neill et al., 2012) during the CCGS Amundsen cruise of August 2009. Therefore, this set of measurements was used to calculate the extinction effects associated in August 2009 with the BFF smoke particles transported from the North American forests over the Arctic

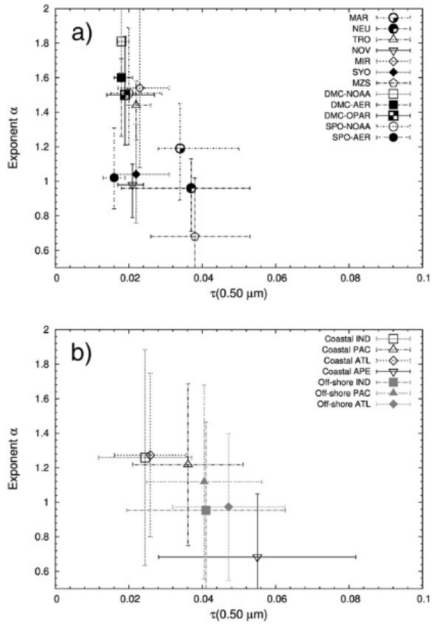

Fig. 13. Part (a): as in Fig. 8, but for the sun-photometer measurements listed in Table 2. Acronym key: Marambio (MAR), Neumayer (NEU), Troll (TRO), Novolazarevskaya (NOV), Mirny (MIR), Syowa (SYO), Mario Zucchelli (MZS), Dome Concordia (DMC-NOAA, DMC-AER, and DMC-OPAR, for the measurement sets collected by GMD/NOAA, AERONET and OPAR groups, respectively (see Table 4)) and South Pole (SPO-NOAA and SPO-AER, for the measurement sets collected by GMD/NOAA and AERONET groups, respectively). Part (b): as in part (a), for the Microtops sun-photometer measurements performed in Antarctic coastal (open symbols) and off-shore areas (solid symbols) during the cruises conducted in the four following oceanic sectors: (i) IND (Southern Indian Ocean, squares), (ii) PAC (Southern Pacific Ocean, upward triangles), (iii) ATL (Southern Atlantic Ocean, diamonds), and (iv) APE (Antarctic Peninsula, downward triangles).

Ocean. In order to study the aerosol extinction features of the Arctic Ocean, the 14 Microtops sun-photometer data-sets collected during the above-selected MAN cruises were subdivided into three sub-sets pertaining to the following large-scale oceanic sectors: (a) Northern Greenland Sea and Norwegian Sea (hereinafter referred to as GNS sector), between 20° W and 30° E longitudes; (b) Barents Sea and West Siberian Sea (BWS sector), between 30° E and 130° E longitudes; and (c) the North American Arctic Ocean (NAA sector), including the East Chukchi Sea, the Bering Strait, the Beaufort Sea and the Amundsen Gulf, between 170° W and 110° W longitudes. No MAN cruises were carried out in the East Siberian Sea and West Chukchi Sea sectors, at latitudes higher than 67° N and longitudes ranging from 130° E to 170° W, as well as in the Canadian sector from 110° W to 20° W longitudes, including the Baffin Bay, the Davis Straits and the Northern Atlantic Ocean.

The same criteria as used for the ground-based stationary sun-photometer measurements taken at the various Arctic sites were also adopted to examine the ship-borne measurements, including the selection of data made to reject all the measurements affected by stratospheric volcanic particle extinction. The daily mean values of $\tau(0.50\ \mu m)$ and α obtained from the data-sets collected within each of the three oceanic sectors were subdivided into monthly sub-sets to determine the monthly mean values of both parameters, and define their RFHs separately for the winter–spring (Arctic haze) and summer–autumn (background aerosol) periods. The main purpose of the analysis was to provide evidence of the seasonal characteristics of aerosol optical parameters in the Arctic Ocean areas far from anthropogenic aerosol sources.

3.1.1. Northern Greenland Sea and Norwegian Sea

Monthly mean values of $\tau(0.50\ \mu m)$ and α derived from the Microtops measurements performed during nine cruises made in the Norwegian Sea, west of Spitsbergen, and one cruise in the northern Greenland Sea and Norwegian Sea are shown in Fig. 14a. Values of $\tau(0.50\ \mu m)$ gradually decreased from less than 0.10 in April to nearly 0.05 in August, with values of σ_τ b 0.03 over the entire period. The monthly mean values of α were rather stable from April to August, ranging from 1.20 to 1.30, with values of σ_α equal to 0.10 in spring and 0.40 in summer. These features suggest that the columnar aerosol content was mixed in spring, consisting of anthropogenic (Arctic haze) and natural sea-salt aerosols, and contained sea-salt aerosol mixed with BFF smoke particles in summer. In fact, the aerosol extinction parameters measured in spring and summer with the Microtops sun-photometers turn out to be very similar to those determined at Ittoqqortoormiit and Hornsund from the AERONET sun-photometer measurements, during spring (when polluted air masses are mainly transported from Europe) and summer (when polar air masses are transported from the Arctic land and oceanic regions towards the Svalbard Archipelago) (Rozwadowska and Sobolewski, 2010; Rozwadowska et al., 2010). These variable features can be more clearly seen by considering the seasonal RFHs of $\tau(0.50\ \mu m)$ and α shown in Fig. 14b, derived from the measurements taken on 77 measurement days in the Greenland Sea and Norwegian Sea (GNS) sector. The RFH of $\tau(0.50\ \mu m)$ exhibits a large peak over the 0.02–0.20 range, with a mean value equal to 0.075, and 25th and 75th percentiles equal to 0.054 and 0.094, respectively, indicating significant variations even in the remote Arctic Ocean. The corresponding RFH of α is also rather wide, showing a mean value of 1.23, and 25th and 75th percentiles equal to 1.02 and 1.47, respectively, as a result of the combination of natural maritime and anthropogenic/continental aerosol loads. It is worth noticing that the GNS average values of $\tau(0.50\ \mu m)$ and α agree fairly well with those determined at Ittoqqortoormiit (Fig. 5) and Hornsund (Fig. 6) and exhibit similar relationships between α and $\tau(0.50\ \mu m)$ to those of the above-mentioned AERONET stations (compare Fig. 8a with those of Fig. 8b).

3.1.2. Barents Sea and West Siberian Sea

Only the RV Polarstern 2012 cruise crossed the Barents Sea and West Siberian Sea (BWS) sector, in August 2012, at latitudes varying from 80° N to 84° N and longitudes ranging from 28° E to 120° E (see Fig. 2). Thus, the monthly mean values of $\tau(0.50\ \mu m)$ and α were only calculated for three measurement days, giving statistically poor values of $\tau(0.50\ \mu m) = 0.054 \pm 0.010$ and $\alpha = 1.42 \pm 0.33$. As noted in Fig. 14a, the above value of $\tau(0.50\ \mu m)$ closely agrees with that measured within the GNS sector on the same month, and α is slightly higher than that measured in August within the same sector. Such results are typical of an oceanic area during relatively calm wind periods.

3.1.3. North American Arctic Ocean

Within the North American Arctic (NAA) oceanic sector, including the East Chukchi Sea, Bering Strait, Beaufort Sea and Amundsen Gulf, only four cruises were considered among those reported in Table 3. The time-patterns of the monthly mean values of $\tau(0.50\ \mu m)$ and α calculated over the March–September period are shown in Fig. 14a. Monthly mean value of $\tau(0.50\ \mu m)$ were about 0.10 in March, peaked in April and May at 0.17 and 0.20, respectively, and decreased in the summer months to 0.10 in June and 0.05 in September. No pronounced variations in α were obtained, with values from 0.90 to 1.20 from March to September, and σ_α varying from 0.20 (in April) to 0.50 (in July). An overall number of 58 measurement days was collected in this oceanic sector over the 7-month period from March to September, for which

Table 3
List of the 14 cruises undertaken in the Arctic oceanic regions by various managing institutions in different geographical areas (at latitudes N67° N), where the ship-borne Level 2.0 sun-photometer measurements of the Maritime Aerosol Network (MAN) programme were conducted from 2003 to 2012, using hand-held Microtops sun-photometers calibrated at the NASA/GSFC calibration facility (Smirnov et al., 2009, 2011). The peak wavelengths of the narrow-band interference filters mounted on the instruments are given, together with the names of the sun-photometer measurement P.I.s.

Cruises and sun-photometer managing institutions	Geographical area	Overall number of measurement days	Measurement period	Peak wavelengths (nm) of the spectral channels used to measure aerosol optical thickness $\tau(\lambda)$	Principal investigator and references
RV Oceania 2003 (IOPAS, Sopot, Poland)	Norwegian Sea, west Spitsbergen 69°–79° N, 2°–14° E	5	June–July 2003	440, 500, 675, 870	T. Zielinsky (Tomasi et al., 2007)
RV Oceania 2006 (IOPAS, Sopot, Poland)	Greenland Sea and Norwegian Sea, 69°–79° N, 15° W–14° E	6	June–July 2006	440, 500, 675, 870	T. Zielinsky (Tomasi et al., 2007)
RV Oceania 2007 (IOPAS, Sopot, Poland)	Norwegian Sea, 69°–78° N, 1°–16° E	6	July 15–August 11, 2007	440, 500, 675, 870	T. Zielinsky
CCGS Louis St. Laurent 2007 (Wood Hole Oceanographic Institution, Woods Hole, Massachusetts, USA)	Beaufort Sea, 70°–79° N, 125°–150° W	9	July 28–August 25, 2007	440, 500, 675, 870	A. Proshutinsky
RV Knorr 2008 (PMEL, NOAA, Seattle, Washington, USA)	Norwegian Sea, 70°–71° N, 19°–31° E	4	April 6–10, 2008	440, 500, 675, 870	P. K. Quinn
CCGS Amundsen 2008 (Institut Maurice-Lamontagne, Mont-Joli, Quebec, Canada)	Beaufort Sea, 70°–73° N, 121°–131° W	43	March 16–August 2, 2008	440, 500, 675, 870	P. Larouche
RV Jan Mayen 2009 (IMEDEA, Esporles, Mallorca, Spain)	Norwegian Sea, 76°–80° N, 11°–28° E	4	June 18–22, 2009	440, 500, 675, 870	C. Duarte
RV Oceania 2009 (IOPAS, Sopot, Poland)	Norwegian Sea, 73°–79° N, 3°–16° E	11	June 23–July 13, 2009	440, 500, 675, 870	T. Zielinsky
CCGS Amundsen 2009 (Université du Québec, Rimouski, Québec, Canada)	Beaufort Sea, 70°–72° N, 127°–135° W	9	July 31–August 25, 2009	440, 500, 675, 870	S. Bélanger
RV Oceania 2010 (IOPAS, Sopot, Poland)	Norwegian Sea, 68°–80° N, 0°–13° E	9	July 6–August 17, 2010	380, 440, 500, 675, 870	T. Zielinsky
RV Oceania 2011 (IOPAS, Sopot, Poland)	Norwegian Sea, 69°–79° N, 3°–19° E	10	June 17–August 13, 2011	440, 500, 675, 870	T. Zielinsky
USCGC Healy 2011 (Naval Research Laboratory, Monterey, California, USA)	Eastern Chukci Sea, Beufort Sea and Arctic Canadian Ocean, 71°–79° N, 142°–165° W	6	August 18–September 24, 2011	440, 500, 675, 870	E. A. Reid
RV Oceania 2012 (IOPAS, Sopot, Poland)	Norwegian Sea, 73°–78° N, 10°–20° E	7	June 27–July 31, 2012	440, 500, 675, 870	T. Zielinsky
RV Polarstern 2012 (Institute of Environmental Physics, University of Bremen, Bremen, Germany)	Norwegian Sea, Barents Sea and West Siberian Sea, 70°–84° N, 18°–109° E	5	August 2–22, 2012	440, 500, 675, 870	L. Istomina

calculations of the RFHs were made, illustrating a statistically robust data-set. The RFH of $\tau(0.50\ \mu m)$ showed a more dispersed distribution curve over the 0.02–0.25 range than that determined for the GNS sector, with a mean value of 0.16, which was considerably higher than that measured in the GNS sector, and also had wider right-hand wings. The RFH of α exhibits a similar shape to that determined in the GNS sector, with a mean value close to 1.10.

The median values and the 25th and 75th percentiles of parameters $\tau(0.50\ \mu m)$ and α were calculated for the sets of daily mean values derived from the Microtops sun-photometer measurements conducted over the GNS, BWS and NAA sectors. The results are shown in Fig. 8b for an easier comparison with those derived from the ground-based sun-photometer measurements conducted at Arctic sites. The ship-borne measurements provided median values of $\tau(0.50\ \mu m)$ ranging from 0.04 to about 0.13, which are therefore comparable with the mean background extinction parameter measured in summer at the ground-based stations. The ship-borne median values of α varied mainly from 1.10 to 1.50, and were appreciably lower than those measured in summer–autumn at the land stations: the scatter plot shown in Fig. 8b provides clear evidence of the prevailing oceanic origins of these aerosol loads.

3.2. Aerosol measurements in the Antarctic Ocean

Eighteen AERONET/MAN cruises were conducted from 2006 to early 2013 over the Antarctic Oceans. They are listed in Table 4, together with the geographical areas covered by the various cruises, the number of measurements days (see also Fig. 2), the measurement periods and the spectral characteristics of the portable Microtops sun-photometers onboard the vessels. To analyse the aerosol optical parameters more homogeneously, the sun-photometer data-sets recorded during the 18 cruises were subdivided into the following four sub-sets: (1) the Southern Indian Ocean (IND) sector, between 20° E and 150° E longitudes; (2) the Southern Pacific Ocean (PAC) sector, between 150° E and 75° W longitudes; (3) the Southern Atlantic Ocean (ATL) sector, between 50° W and 20° E longitudes; and (4) the oceanic region around the Antarctic Peninsula (APE), between 75° and 50° W longitudes. The daily mean values of $\tau(0.50\ \mu m)$ and α measured with the portable Microtops sun-photometers calibrated at NASA/GSFC facility (Smirnov et al., 2009, 2011) were analysed separately for coastal data (for distances smaller than 300 km from the Antarctic coast) and off-shore data (for distances of 300 to 1000 km from the coast), according to the criteria used by Wilson et al. (2010) to distinguish the data related to a significant landmass from those of pure oceanic origin (i.e., given for the large part by maritime aerosols generated by wind-related sources). The overall set of Microtops data was then examined following the same criteria adopted to analyse the Arctic ship-borne measurements, separately for the above-mentioned four oceanic sectors.

3.2.1. Southern Indian Ocean

As can be seen in Table 4, eleven cruises were conducted in the Southern Indian Ocean, during periods from December to March in the years from 2005/2006 to 2011/2012, collecting an overall set of 226 coastal measurement days, and only nine off-shore measurement days (see Fig. 2). The time-patterns of the monthly mean values of $\tau(0.50\ \mu m)$ and α are shown in Fig. 15a for coastal and off-shore data. AOT values of $\tau(0.50\ \mu m)$ were rather stable from December to April over the coastal areas, varying from 0.010 to 0.025, with $\sigma_\tau = \pm 0.01$ on average, and were appreciably greater over the off-shore area, being close to ~0.06 in January, 0.04 in November and December, and

Table 4
List of the 18 cruises undertaken in the Antarctic oceanic regions by various managing institutions in different geographical areas (at latitudes N62° S), where the ship-borne sun-photometer measurements of the Maritime Aerosol Network (MAN) programme were conducted from 2005/2006 to 2012/2013 in the austral summer months, using hand-held Microtops sun-photometers calibrated at the NASA/GSFC calibration facility (Smirnov et al., 2009, 2011). The peak wavelengths of the narrow-band interference filters mounted on the instruments are given, together with the names of the sun-photometer measurement P.I.s.

Cruises and sun-photometer managing institution	Geographical area	Overall number of measurement days	Measurement period	Peak wavelengths (nm) of the spectral channels used for measuring aerosol optical thickness $\tau(\lambda)$	Principal investigator
RV Akademik Fedorov 2005/2006 (IAO-SB-RAS, Tomsk, Russia)	Southern Indian Ocean 65°–70° S, 44°–93° E	20	December 20, 2005–January 26, 2006	340, 440, 500, 675, 870	S. M. Sakerin
RV Akademik Fedorov 2006/2007 (IAO-SB-RAS, Tomsk, Russia)	Southern Indian Ocean 65°–69° S, 46°–93° E	40	December 13, 2006–March 4, 2007	340, 440, 500, 675, 870	S. M. Sakerin
MV SA Agulhas 2007/2008 (Climatology Research Group, University of Witwatersrand, Johannesburg, South Africa)	Southern Atlantic Ocean, 68°–70° S, 2° W–4° E	15	December 18, 2007–January 10, 2008	440, 500, 675, 870	S. Piketh (Wilson et al., 2010)
RV Akademik Fedorov 2007/2008 (IAO-SB-RAS, Tomsk, Russia)	Southern Indian Ocean, 66°–69° S, 45° E–95° E	18	December 14, 2007–January 4, 2008	440, 500, 675, 870	S. M. Sakerin
	Southern Pacific Ocean, 68°–72° S, 90°–163° W	14	January 24–February 17, 2008		
	Antarctic Peninsula, 63°–65° S, 60°–45° W	3	February 20–24, 2008		
	Southern Atlantic Ocean, 65°–70° S, 50°W–15° E	13	March 25–April 22, 2008		
RV Akademik Fedorov 2008/2009 (IAO-SB-RAS, Tomsk, Russia)	Southern Indian Ocean, 66°–69° S, 76°–93° E	11	December 22, 2008–January 6, 2009; January 25–March 23, 2009	440, 500, 675, 870	S. M. Sakerin
	Southern Pacific Ocean, 67° S, 161° E	1	January 17, 2009		
Vessel RV Astrolabe 2009/2010 (OPAR, Univ. de Reunion, Reunion, France)	Southern Indian Ocean 66°–67° S, 140°–141° E	5	January 5–23, 2010	440, 500, 675, 870	Y. Courcoux
RV Akademik Fedorov 2009/2010 (IAO-SB-RAS, Tomsk, Russia)	Southern Indian Ocean, 65°–70° S, 70°–100° E	12	December 15, 2009–January 4, 2010; March 30–April 6, 2010	440, 500, 675, 870	S. M. Sakerin
	Southern Pacific Ocean 65°–75° S, 87°–172° W	7	January 19–28, 2010		
	Antarctic Peninsula, 62° S, 59° W	1	February 6, 2010		
Prince Albert II 2010 (Space Physics Laboratory, University of Kyiv, Kyiv, Ukraine)	Antarctic Peninsula 62°–67° S, 58°–67° W	11	January 9–February 17, 2010	440, 500, 675, 870	G. Milinevsky
NP Almirante Maximiano 2010/2011 (Rio de Janeiro State University, Rio de Janeiro, Brazil)	Antarctic Peninsula 62°–64° S, 56°–61° W	7	January 7–March 21, 2011	440, 500, 675, 870	H. Evangelista
RV Akademik Fedorov 2010/2011 (AARI, St. Petersburg, Russia)	Southern Indian Ocean 65°–69° S, 45°–93° E	18	December 18, 2010–February 2, 2011	440, 500, 675, 870	V. F. Radionov
RV Astrolabe 2011 (OPAR Institute, Univ. de la Réunion, Saint Denis de la Réunion, France)	Southern Indian Ocean 67° S, 140° E	24	January 5–March 1, 2011	340, 440, 500, 675, 870	Y. Courcoux
MV SA Agulhas 2011/2012 (Climatology Research Group, University of Witwatersrand, Johannesburg, South Africa)	Southern Atlantic Ocean 67°–71° S, 0°–9° W	17	December 19, 2011–February 13, 2012	340, 440, 500, 675, 870	S. Broccardo
NP Almirante Maximiano 2011/2012 (Rio de Janeiro State University, Rio de Janeiro, Brazil)	Antarctic Peninsula, 61°–62° S, 55°–59° W	6	October 24, 2011–November 14, 2011	440, 500, 675, 870	H. Evangelista
RV Akademik Fedorov 2011/2012 (AARI, St. Petersburg, Russia)	Southern Indian Ocean 66°–69° S, 37°–93° E	19	December 12, 2011–March 21, 2012	440, 500, 675, 870	V. F. Radionov
	Southern Atlantic Ocean 62°–70° S, 18° W–20° E	8	March 22–April 7, 2012		
	Antarctic Peninsula 62.2° S, 58.9° W	2	April 21 and 22, 2012		
RV Astrolabe 2012 (OPAR Institute, Univ. de la Réunion, Saint Denis de la Réunion, France)	Southern Indian Ocean 66° 40′ S, 140° E	14	February 20–March 2, 2012	380, 440, 500, 675, 870	Y. Courcoux
RV SA Agulhas II 2012/2013 (Climatology Research Group, University of Witwatersrand, Johannesburg, South Africa)	Southern Atlantic Ocean 70°–71° S, 1°–8° W	11	December 19, 2012–February 5, 2013	380, 440, 500, 675, 870	S. Broccardo
RV Akademik Fedorov 2012/2013 (AARI, St. Petersburg, Russia)	Southern Indian Ocean 66°–70° S, 46°–93° E	24	December 13, 2012–March 15, 2013	440, 500, 675, 870	V. F. Radionov
	Southern Atlantic Ocean 67°–70° S, 10°–12° E	3	March 22–24, 2013		
RV Akademik Treshnikov 2012/2013 (AARI, St. Petersburg, Russia)	Antarctic Peninsula, 64°–70° S, 57°–72° W	13	February 11–March 5, 2013	440, 500, 675, 870	V. F. Radionov

0.02 in February. The coastal values of α varied from 1.20 to 1.40 in the December–April period, while the off-shore values decreased from 1.20 to less than 0.60 from November to December, and then slowly increased to around 0.90 in February. These findings give a measure of the increase in $\tau(\lambda)$ and the variations in α, which are observed passing from coastal to off-shore areas as a result of the stronger production of sea-salt coarse particles. The daily mean values of $\tau(0.50\ \mu m)$ and α were derived over the Southern Indian Ocean on 226 measurement days near the Antarctic coasts, and on only nine days in off-shore areas. Therefore, only the RFHs of the coastal daily mean values of $\tau(0.50\ \mu m)$ and α have been analysed: the RFH of $\tau(0.50\ \mu m)$ shown in Fig. 15b presents a very narrow curve, with a mean value of 0.024, and 25th and 75th percentiles very close to the mean, while the RFH of α exhibits a broad curve, with a mean value of 1.20 and 25th and

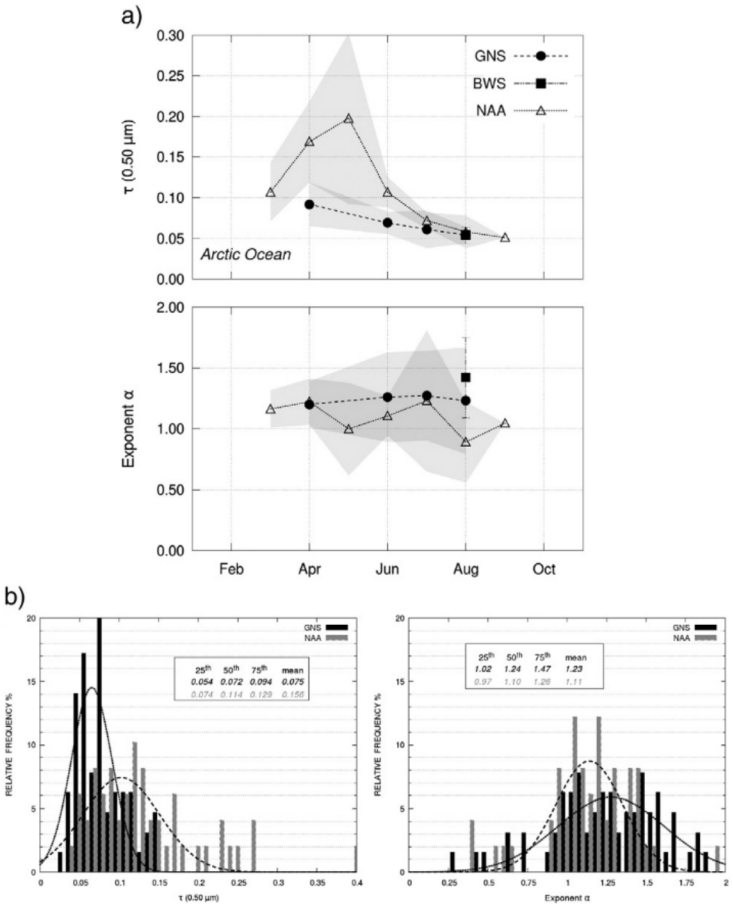

Fig. 14. Part (a): as in Fig. 3, for Microtops sun-photometer measurements of aerosol optical thickness $\tau(0.50\,\mu m)$ and exponent α performed during the cruises conducted from 2003 to 2012 in the GNS (Greenland Sea and Norwegian Sea) sector (solid circles), from 2006 to 2012 in the BWS (Barents Sea and West Siberian Sea) sector (solid squares), and from 2008 to 2011 in the NAA (Eastern Chuckci Sea, Beaufort Sea and Amundsen Gulf) sector (open triangles) (see also Table 3). Part (b): relative frequency histograms of the daily mean values of aerosol optical thickness $\tau(0.50\,\mu m)$ and exponent α determined from the Microtops measurements conducted from March to September over the GNS (Greenland Sea and Norwegian Sea) sector, and the NAA (North American Arctic Ocean) sector, including the Eastern Chuckci Sea, Beaufort Sea and Amundsen Gulf.

75th percentiles equal to 0.84 and 1.51. These findings clearly indicate that a large variability characterises the sea-salt accumulation and coarse mode particle concentrations in coastal areas.

3.2.2. Southern Pacific Ocean

As reported in Table 4, only three AERONET/MAN cruises were conducted in the Southern Pacific Ocean over the December–January periods of 2007/2008 to 2009/2010, over the area defined in Fig. 2, giving an overall number of 20 coastal and 5 off-shore measurement days. The monthly mean values of $\tau(0.50\,\mu m)$ and α varied from 0.03 to 0.04 near the coasts, and from 0.04 to 0.05 in the off-shore areas, while the coastal monthly mean values of α decreased from ~1.45 in December to ~1.00 in January, and the off-shore values from 1.40 to 0.70. The values of $\tau(0.50\,\mu m)$ and α result to closely agree with those measured at Neumayer, Novolazarevskaya, Mirny, Syowa, and Mario Zucchelli, shown in Figs. 9–12. A coastal median value of $\tau(0.50\,\mu m)$ equal to ~0.04 was obtained, with the main percentiles differing by less than 0.02, while the median value of α was equal to 1.20, with the main percentiles differing by about 0.50. The off-shore data-set provided a similar value of $\tau(0.50\,\mu m)$ and more distant main percentiles, with a median value of $\alpha = 1.15$, and main percentiles differing by more than 0.40.

3.2.3. Southern Atlantic Ocean

A large set of AERONET/MAN sun-photometer measurements was collected in the Southern Atlantic Ocean during five cruises conducted in 2007/2008, 2011/2012 and 2012/2013, as reported in Table 4, giving 63 coastal and only 8 off-shore measurement days. The monthly mean values of $\tau(0.50\,\mu m)$ varied from 0.03 in December to less than 0.02 in April, with $\sigma_\tau = 0.01$ on average, while those of α increased from ~1.10 in December to 1.50 in February, and then decreased to 1.30 in April. The RFH of the coastal $\tau(0.50\,\mu m)$ values was found to exhibit similar features to those determined in the coastal area of the Antarctic Indian Ocean, with a leptokurtic shape having a mean value of 0.025

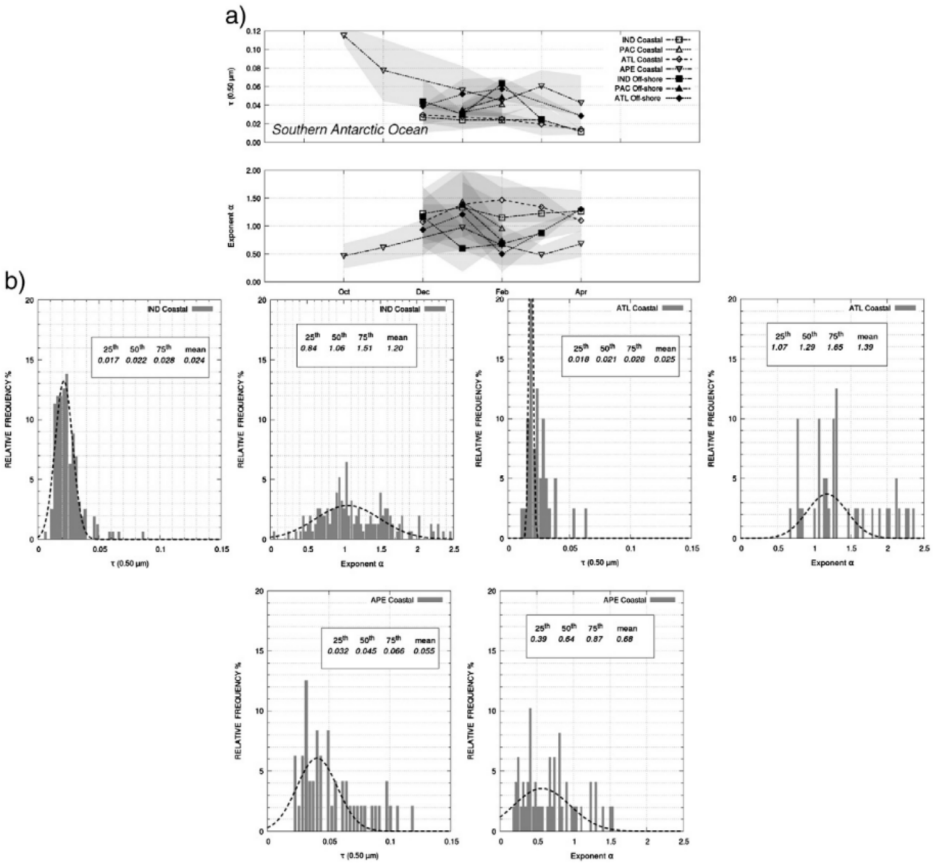

Fig. 15. Part (a): as in Fig. 3, for Microtops sun-photometer measurements of $\tau(0.50\ \mu m)$ and α performed during the cruises conducted from late 2005 to spring 2013 in the frame of the Maritime Aerosol Network (MAN) activities listed in Table 4. The data refer to coastal (open symbols) and off-shore (solid symbols) measurements, carried out in the IND sector (Southern Indian Ocean, circles), PAC sector (Southern Pacific Ocean, upward triangles), ATL sector (Southern Atlantic Ocean, squares), and APE sector (Antarctic Peninsula, downward triangles). Part (b): Relative frequency histograms of $\tau(0.50\ \mu m)$ and α obtained for the coastal data-sets collected (i) on 226 measurement days from November to February over the Southern Indian Ocean (IND) sector; (ii) 63 measurement days from December to April over the Southern Atlantic Ocean (ATL) sector; and (iii) on 49 measurement days from October to April over the coastal area surrounding the Antarctic Peninsula (APE sector).

and the 25th and 75th percentiles differing by less than 0.01, while the RFH of α showed a rather broad shape over the 0.5–2.4 range, with a mean value of 1.39 and the 25th and 75th percentiles differing by about 0.30, thus being similar to that determined for the Pacific Ocean coastal data-set.

3.2.4. Around the Antarctic Peninsula

Numerous aerosol optical data were collected in coastal areas surrounding the Antarctic Peninsula during the seven AERONET/MAN cruises conducted from 2007/2008 to 2012/2013, as reported in Table 4, collecting an overall number of 49 measurement days, not far from the coasts. The time-patterns of monthly mean values of $\tau(0.50\ \mu m)$ and α obtained from these measurements are shown in Fig. 15b. A very high value of $\tau(0.50\ \mu m)$ close to 0.12 was obtained in October, followed by decreasing monthly mean values equal to 0.08 in November and lower than 0.06 in December, and then varying from 0.04 to 0.06 over the January–March period, with $\sigma_\tau = 0.02$ on average. The monthly mean values of α were all rather low, varying from 0.50 to 1.00 over the October–February period, with $\sigma_\alpha = 0.20$ on average. The exceptionally high monthly mean values of $\tau(0.50\ \mu m)$ were determined in October and November for measurement days giving values of α varying from 0.24 to 0.69, and presenting prevailing transport of air masses from the off-shore areas of the Drake Passage. Similar aerosol optical characteristics were observed by Posyniak and Markowicz (2009) for flows from the North-Eastern quadrant, accompanied by low visibility conditions because of the transport of large amounts of sea-salt particles from the Drake Passage, with wind speed N10 m/s. Relatively low daily mean values of α were measured on these days, ranging from 0.43 to 0.73, due to maritime aerosols generated by the strong winds, which dominated extinction. For southerly wind circulation, considerably lower values of $\tau(0.50\ \mu m)$ were measured in this coastal area. Therefore, because of the large variability of wind directions, the RFH of $\tau(0.50\ \mu m)$ determined over the October–March period exhibited rather dispersed features, with a mean value of ~0.05 and the 25th and 75th percentiles differing by less than 0.02. These evaluations are higher by about a factor 2 than those obtained over the coastal areas of the Indian and Atlantic Oceans, because of the more significant contribution of sea-salt accumulation and coarse mode particles generated by

stronger winds. The RFH of α shows a rather broad shape over the range α b 1.5, with a mean value close to 0.70, which is about half of that measured over the Indian and Atlantic Ocean coastal areas, and the 25th and 75th percentiles differing by no more than 0.30, due to the predominant extinction by maritime particles.

The above results obtained from the coastal and off-shore data recorded over the four sectors of the Southern Antarctic Ocean are characterised by features of τ(0.50 μm) and α typical of sea-salt maritime particles, as can be clearly seen in Fig. 13b, in which the median values of α are plotted versus the median values of τ(0.50 μm), separately for the coastal and off-shore data. The comparison between these results and the scatter plot shown in Fig. 13a shows that they are very similar to those derived from the sun-photometer measurements conducted at the coastal Antarctic stations, since the cluster derived from the AERONET/MAN measurements of α and τ(0.50 μm) essentially covers the same domain of the ground-based measurements recorded at Marambio, Novolazarevskaya, Syowa, Neumayer, and Mario Zucchelli, although exhibiting slightly lower values of α.

4. Aerosol backscattering coefficient profiles from lidar measurements

Lidar sends a light pulse through the atmosphere and the telescope collects the backscattered lidar return signal. As the speed of light is known, one can easily calculate the exact atmospheric position, from which the lidar signal has originated. Therefore, the determination of aerosol vertical structure is possible, at least over the altitude range in which the image of the laser is completely within the field-of-view of the recording telescope. Lidar pulses can be generated at several wavelengths and polarisation elements can also be used at the point of light entrance to the telescope. This enables a determination of the shape of scatterers because spherical particles do not depolarise light, while non-spherical particles normally do.

Overcoming the considerable operational and logistic difficulties, various lidar systems have been deployed in the polar regions to measure: (i) the vertical profiles of backscatter and extinction coefficients of the various aerosols, cloud droplets and ice-crystals, as well as their microphysical and radiative characteristics; (ii) the vertical distribution of temperature and water vapour mixing ratio; and (iii) the ozone concentration at stratospheric levels, to more thoroughly investigate the role of Polar Stratospheric Clouds in destroying ozone molecules at polar latitudes. Actually, most of these measurements were conducted to study the dynamic features of the ozone hole in Antarctica and ozone depletion in the Arctic region associated with the polar vortex occurrences, and the physical characteristics of tropospheric clouds, while relatively few measurement campaigns were specifically conducted with lidar techniques to investigate the optical characteristics of tropospheric aerosols at polar latitudes. An exhaustive description of the lidar measurements conducted in polar regions over the past few decades was recently made (Nott and Duck, 2011). Lidar activities were conducted in the Arctic at the following sites:

(i) Barrow (Northern Alaska), where long-term lidar measurements were recorded and a micropulse lidar is currently used to carry out cloud climatology studies that have evaluated average seasonal cloud occurrences of 65% in winter, 68% in spring, 83% in summer, and 89% in autumn, with an annual mean decrease of − 4.8% per year over the past 10 years (Dong et al., 2010).

(ii) Eureka (Nunavut, Canada), where an elastic lidar was used from 1993 to 1997 to carry out winter-time aerosol measurements for studying the occurrences of clouds and Arctic haze. Backscatter peaks due to haze particle layers were frequently observed at altitudes lower than 3 km, and more occasionally at altitudes of 3–5 km, for relative humidity b60% over ice, while clouds dominate at N80% over ice. Spectral measurements of the aerosol backscatter coefficient $\beta_{bs}(\lambda)$ and depolarisation ratio $\delta_V(\lambda)$ were regularly conducted from 2005 to 2010, over the height range from 70 m up to approximately 15 km, using a High Spectral Resolution Lidar (HSRL) of the University of Wisconsin (USA), at the wavelengths 0.532 and 1.064 μm, for the aerosol backscatter coefficient $\beta_{bs}(\lambda)$, and 0.532 μm only for $\delta_V(\lambda)$ and $\beta_{ext}(\lambda)$. This lidar system was used together with a millimetre cloud radar to classify the various cloud particle types. Since 2008, a troposphere ozone DIAL (Differential Absorption Lidar) and a Raman lidar have been operated simultaneously, equipped with aerosol channels in the visible and ultraviolet light and water vapour and rotational Raman temperature channels.

(iii) Alert (Nunavut, Canada), where an elastic lidar was operated in 1984–1986 to measure the vertical profiles of aerosol backscatter coefficient.

(iv) Summit (Central Greenland), where a depolarisation lidar and a micropulse lidar were used since 2010, to characterise the aerosol types suspended over the Greenland ice sheet.

(v) Ny-Ålesund (Spitsbergen, Svalbard), where various lidar models were used, such as: (a) a stratospheric lidar since 1988; (b) the KARL (Koldewey-Aerosol-Raman Lidar) since 1999, this system being equipped with aerosol channels, depolarisation and ultraviolet and visible water vapour channels, and subsequently rebuilt in 2008 with enhanced multi-wavelength aerosol channels to cover the 0.45–30 km altitude range; and (c) an automated micropulse lidar (Hoffmann et al., 2009) since 2003, as a part of the MPLNET and NDACC networks, which provided cloud and aerosol measurements in March and April 2007, useful to characterise air masses as a function of depolarisation and backscatter ratios.

(vi) Hornsund (Spitsbergen, Svalbard), where an automated lidar has been operated since 2009, to measure the vertical profiles of volume extinction coefficient β_{ext}(0.532 μm) produced by aerosols during transport episodes of unpolluted air masses from the Greenland Sea and Norwegian Sea areas; and

(vi) Andøya Rocket Range (Arctic Lidar Observatory for Middle Atmosphere Research, ALOMAR), near Andenes (Northern Norway), where a tropospheric lidar was installed in 2005 and a polarisation-sensitive bistatic lidar system has been used since 2006 to study the vertical distribution features of polar aerosols and their optical characteristics.

The above-mentioned field measurements provided vertical profiles of the most significant aerosol scattering parameters, illustrating that the Arctic haze particles are in general present below the 3 km level during severe haze events, and occasionally at 3–5 km altitudes, as shown by the measurements conducted at Eureka (Nott and Duck, 2011). During the dense haze episode observed with the KARL lidar at Ny-Ålesund on May 2, 2006, strong extinction features were recorded from the ground up to 2.5 km altitude, which showed multi-layered profiles of the aerosol backscattering coefficient β_{bs}(0.532 μm) decreasing on average from 3.5 km^{-1} near the ground to below 0.5 km^{-1} at 2.5 km altitude. Conversely, for unpolluted air conditions, the scale height of β_{bs}(0.532 μm) was often found to vary from 1.0 to 1.3 km at Ny-Ålesund, as estimated for instance by Hoffmann et al. (2012) who examined the backscatter ratio measurements conducted with the KARL lidar over the whole of 2007.

However, so far our knowledge of Arctic haze from a lidar point of view is still incomplete, because the majority of published results are based on case studies. Therefore, the yearly cycle of aerosols has been studied in this paper on the basis of the lidar measurements conducted at Ny-Ålesund over the period from 1 November, 2012, to 31 October, 2013, examining the overall set of KARL lidar measurements taken without cloud interferences and with resolutions of 60 m in height and 10 min in time, according to Ansmann et al. (1992). To guarantee a homogeneous data-set, only lidar profiles with identical technical settings have been considered. Moreover, cloud screening was conducted

and the lowest 800 m were removed from the analysis due to overlap (Weitkamp, 2005). Finally, the data derived from the Vaisala RS-92 radiosonde data collected at the site have been used to subtract the Rayleigh backscatter coefficient from the lidar data. The fact that the time of the lidar observation does not coincide with the launch of the radiosonde should cause errors no higher than 5% in evaluating the aerosol backscatter coefficient. This is probably even an upper bound, since Rogers et al. (2011) only estimated a 3% bias for the CALIOP (Cloud-Aerosol Lidar with Orthogonal Polarization) lidar on board the CALIPSO satellite. Fig. 16 shows the monthly averaged profiles of the aerosol volumetric backscatter coefficient $\beta_{bs}(0.532\ \mu m)$ from January to May and the three bi-monthly averaged profiles from June to December, providing evidence of significant variations in this optical parameter throughout the year. A clear annual cycle of the aerosol backscatter coefficient can be seen, which increased in February mainly in the low troposphere and reached its maximum values during March and April in the whole troposphere, subsequently decreasing appreciably in May. The months June to January were relatively clear, always showing appreciably lower values at all altitudes. Another view of the same data is shown in Fig. 17, where the monthly averaged values of $\beta_{bs}(0.532\ \mu m)$ were integrated over five partial height-intervals and the total range from 0.8 to 7.0 km. The results show that the Arctic haze layer starts to form at low altitudes early in the season and lasts until May not only in the low troposphere but also at high altitudes. In fact, the maximum values below 2.5 km altitude have been found in March, while the largest values of $\beta_{bs}(0.532\ \mu m)$ occur in April at 1.5–2.5 km altitudes. It can be also noted in Fig. 17 that the haze season starts more rapidly than it disappears, since the increase in backscatter observed between January and March is steeper, whereas the decline lasts from April till August.

The annual cycle of the lidar ratio $S_a(0.532\ \mu m)$ between the aerosol extinction coefficient $\beta_{ext}(0.532\ \mu m)$ and the aerosol backscatter coefficient $\beta_{bs}(0.532\ \mu m)$ is presented in Fig. 18, separately calculated over the altitude sub-ranges z b 3.5 km and z N 3.5 km and over the whole altitude range, for the KARL lidar measurements conducted from early November 2012 to late October 2013. It shows that $S_a(0.532\ \mu m)$ takes the highest values in June–July and generally increases with altitude. However, its annual cycle is not very pronounced below 3.5 km altitude, where most of the aerosol is located, presenting values varying from 30 to 35 sr. This is typical of clean continental aerosol (Winker et al., 2009). Conversely, the monthly mean values of $S_a(0.532\ \mu m)$ calculated above 3.5 km were estimated to vary from 30 to 40 sr in winter, i.e. assuming values typical of clean continental aerosol and dust, and to increase until reaching surprisingly high values of 60–70 sr in summer, which are normally typical of BFF smoke and polluted continental aerosol. However, one has to keep in mind that the lidar ratio depends not only on the chemical composition but also on the shape and size-distribution of aerosols. It also agrees well with the evaluations of $S_a(0.532\ \mu m)$ made by Ackermann (1998) for different aerosol types suspended in air for relative humidity conditions ranging from 40% to 50%, estimated to be of 27 sr for maritime aerosols and around 55 sr for continental aerosol suspended in relatively dry air masses, like those frequently observed in the polar atmosphere over land (which probably indicate a decrease in the influence of marine air masses with altitude). Due to the contributions of both low and high tropospheric regions, the overall values of $S_a(0.532\ \mu m)$ were estimated to range mainly from 30 to 50 sr.

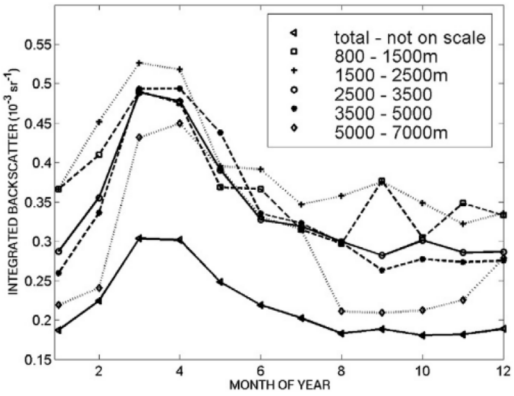

Fig. 17. Time-patterns of the monthly average values of the aerosol volume backscatter coefficient $\beta_{bs}(0.532\ \mu m)$ integrated over the different altitude ranges reported in the legend, as obtained from the KARL lidar measurements performed at Ny-Ålesund (AWIPEV station) from 1 November, 2012, to 31 October, 2013.

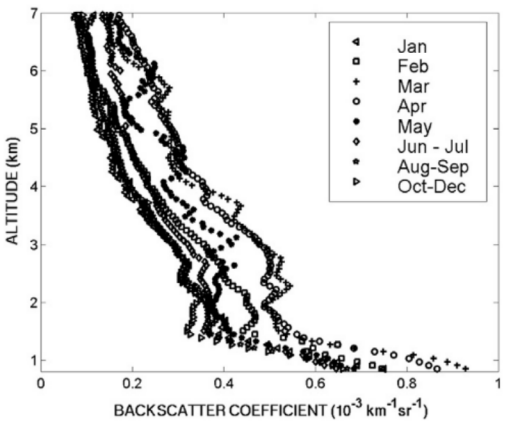

Fig. 16. Monthly and bi-monthly averaged vertical profiles of aerosol volume backscatter coefficient $\beta_{bs}(0.532\ \mu m)$ obtained from the KARL lidar measurements conducted at Ny-Ålesund (AWIPEV station) from 1 November, 2012, to 31 October, 2013.

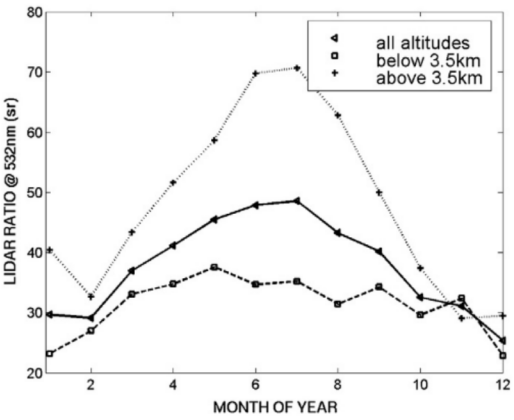

Fig. 18. Time-patterns of the monthly average values of the lidar ratio $S_a(0.532\ \mu m) = \beta_{ext}(0.532\ \mu m)/\beta_{bs}(0.532\ \mu m)$ calculated over the whole altitude range (triangles) and the altitude sub-ranges z b 3.5 km (squares) and z N 3.5 km (+), as obtained from the KARL lidar measurements conducted at Ny-Ålesund (AWIPEV station) from 1 November, 2012, to 31 October, 2013.

To quantify the direct radiative forcing of Arctic haze, it is very important to know the morphological and optical features of atmospheric aerosols, as well as the multimodal size-distribution, the refractive index and the particle shape. The ratio of the perpendicular to parallel polarised backscatter returns from aerosols at a certain wavelength λ gives the volume depolarisation ratio $\delta_V(\lambda)$, which provides an effective range-resolved method of determining whether the laser pulse has been backscattered by spherical or non-spherical aerosols (Winker et al., 2009). Bearing in mind that spherical particles do not depolarise the incoming solar radiation, the scatter plot of the monthly (from January to May) and bi-monthly (from June to December) averaged values of depolarisation ratio percentage are shown in Fig. 19 versus the aerosol backscatter coefficient β_{bs}(0.532 μm), as obtained from the KARL lidar measurements conducted from early November 2012 to late October 2013. Generally quite low values of aerosol depolarisation ratio δ_V(0.532 μm) have been found (appreciably lower for instance than those of desert dust), with the lowest values in January, and values ranging from 2.0% to 2.6% in October–December, over the range of β_{bs}(0.532 μm) b 4.5×10^{-4} km^{-1} sr^{-1}. Remarkably higher depolarisation values, greater than 2.6%, have been found during the maximum of the haze season, in March and April, for values of β_{bs}(0.532 μm) ranging from 4.0×10^{-4} to 5.5×10^{-4} km^{-1} sr^{-1}. This means that the Mie theory, while being a fair assumption to model the forcing of Arctic aerosol during most of the year, is less accurate during spring time.

Lidar measurements were taken at the coastal Antarctic stations of Syowa, Mario Zucchelli, McMurdo and Dumont d'Urville (66° 40′ S, 140° 01′ E), and at the Antarctic Plateau sites of Dome Concordia and South Pole over the past decades (see the Antarctic map in Fig. 2), to monitor the microphysical parameters of clouds at various altitudes (for cloud climatology studies), and only occasionally to measure the vertical profile of the tropospheric aerosol scattering coefficient β_{ext}(0.532 μm). It was found in general that the cloud-free vertical profile of aerosol scattering does not exhibit particularly dense layers near the surface, but shows that β_{ext}(0.532 μm) decreases rapidly with height, to reach the free troposphere "background aerosol" conditions immediately above the marine PBL. The first lidar measurements were conducted during the 1974/1975 austral summer at South Pole, where regular measurements have also been carried out with a micropulse system since 1999, mainly to study the microphysical characteristics of diamond dust and blowing snow events. Ground-based lidar measurements have also been regularly conducted at Dome Concordia since 2007, by using the elastic-backscatter and depolarisation lidar system of the IFAC-CNR Institute (Florence, Italy). Analysis of these data revealed that "diamond dust" ice-crystals are often present during windy conditions at this remote site, within the boundary layer of 100–200 m depth, while aerosols contribute to yield slowly decreasing values of β_{scat}(0.532 μm) with height, until rapidly reaching the background conditions of the free troposphere.

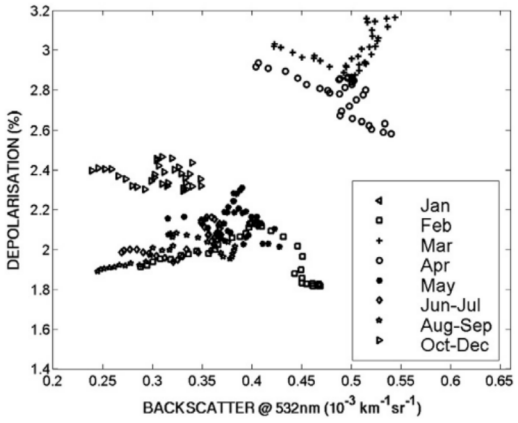

Fig. 19. Scatter plots of the monthly and bi-monthly averaged values of the depolarisation ratio (%) versus the aerosol backscatter coefficient β_{bs}(0.532 μm), as obtained from the KARL lidar measurements conducted at Ny-Ålesund (AWIPEV station) from 1 November, 2012, to 31 October, 2013.

Diamond dust episodes were also frequently observed over the Arctic Ocean. Ground-based lidar and radar were used for this purpose during the Surface Heat Budget of the Arctic Ocean (SHEBA) programme, determining the physical characteristics of diamond dust ice-crystals and assessing the surface radiative effects induced by such particles under cloud-free sky conditions. Examining a set of 188 diamond dust or ice-crystals episodes over the western Arctic Ocean between November 1997 and May 1998, Intrieri and Shupe (2004) found that diamond dust episodes covered about 13% of the time between November and mid-May over the Arctic Ocean and were never observed from mid-May to October. Lidar measurements highlighted that the diamond dust vertical depth varied from 100 m to 1000 m on the various cloud-free sky days, although it was most frequently observed to involve the lower 250 m of the troposphere on average, thus contributing to induce only small radiative effects on the sea ice surface.

Airborne lidar measurements of vertical profiles of aerosol extinction and backscatter coefficients were conducted in the Arctic, over the Svalbard area in spring 2000, 2004 and 2007, during the ASTAR (Arctic Study of Aerosol Clouds and Radiation) campaigns, together with complementary ground-based lidar measurements at Ny-Ålesund (Spitsbergen). The ASTAR 2000 campaign ran from 12 March until 25 April 2000 with extensive flight operations over the Svalbard region using the AWI aircraft POLAR 4. Simultaneous ground-based measurements were conducted at Ny-Ålesund (at both German Koldewey and Japanese Rabben stations as well as at the Zeppelin station). Vertical profiles of various aerosol parameters were measured during the campaign and provided evidence of the strong temporal variability of the Arctic spring aerosol with height. A strong haze event occurred between 21 and 25 March, in which AOT measured from ground-based observation was 0.18, i.e. largely greater than the aerosol background value measured in summer. The airborne measurements made on 23 March showed a high aerosol layer with an extinction coefficient of 0.03 km^{-1} or more up to 3 km. The chemical analyses of airborne measurements showed that such an aerosol transported from anthropogenic sources mainly consisted of sulphate, soot and sea-salt particles (Yamanouchi et al., 2005). Lidar measurements of 532/355 nm colour ratio were obtained by Lampert et al. (2009) during the ASTAR 2007 experiment, indicating the presence of particles with an effective diameter b5 μm. However, Lampert et al. (2010) found rather low Arctic haze levels in spring 2007, examining lidar measurements of cloud and aerosol layers. As pointed out by Hoffmann et al. (2009), the Arctic haze optical thickness τ(0.50 μm) measured during such a seasonal period was evaluated to vary mainly from 0.05 to 0.08, compared to a 14-year average value of 0.10. The PBL extended up to 2.5 km altitude and predominantly contained well-hydrated particles, such as local sea-spray derived sulphates.

Various airborne lidar measurements were conducted as part of the POLARCAT programme during the 2007–2008 International Polar Year, to define the aerosol radiative characteristics. In particular, analysing the backscatter measurements provided by the LEANDRE multichannel lidar mounted on the ATR-42 aircraft, cases of aerosol transport from Europe and Eastern Asia were monitored in April 2008 by de Villiers et al. (2010). These studies showed that anthropogenic aerosols originating in Europe exhibited in general smaller sizes than Asian particles within the PBL below a height of 0.8 km and within layers at heights ranging from 2.8 to 4.5 km, consisting mainly of biomass burning substances and urban/industrial particulate matter, with aerosol

backscatter coefficient β_{bs}(0.532 μm) ranging from 1.2×10^{-3} to 2.2×10^{-3} km^{-1} sr^{-1}, and depolarisation ratio varying from 1.6% to 2.1% (with standard deviations of 0.3% on average). Conversely, the Asian dust plume observed in April 2008 was estimated to contain larger particles, presenting some well-defined aerosol layers at altitudes from 1.7 to 5.6 km, with β_{bs}(0.532 μm) varying from 1.6×10^{-3} to 3.9×10^{-3} km^{-1} sr^{-1}, and depolarisation ratio values equal to 2.0% (smoke particles), 3.0–5.0% (clean continental aerosol), 8.0% (dust), and 4.0–10.0% (polluted dust).

The above results were obtained using also the Level 2.0 products given by the CALIOP lidar mounted on the CALIPSO satellite, which was launched in April 2006 (Winker et al., 2009, 2010) as a part of the A-train constellation of satellites, and has an orbit inclination of 98.2°, thus providing coverage to 82° latitude. This wide coverage has proven immensely important in polar regions, where ground-based installations are few and far between. The CALIOP lidar operates at wavelengths of 0.532 and 1.064 μm, with a depolarisation ratio measured at 0.532 μm, and was used to characterise the various aerosol types by assuming in such an approach a set of values of lidar ratios S_a(0.532 μm) and S_a(1.064 μm) equal to 20 and 45 sr for clean marine aerosol, 35 and 30 sr for clean continental aerosol, 40 and 30 sr for dust, 65 and 30 sr for polluted dust, 70 and 30 sr for polluted continental aerosol, and 70 and 40 sr for combustion smoke particles, respectively (Winker et al., 2009).

A first airborne campaign referred to as the Polar Airborne Measurements and Arctic Regional Climate Model Simulation Project (PAMARCMiP) took place during April 2009 in the Arctic, using a pair of downward-looking lidars, a depolarisation aerosol lidar and a tropospheric ozone DIAL mounted onboard the Polar 5 research aircraft of the Alfred Wegener Institute (AWI) for Polar and Marine Research (Germany). On the basis of the evaluations made by Rogers et al. (2011), it can be assumed that a relative 3% bias of aerosol backscatter coefficient β_{bs}(0.532 μm) was made on average, due to a wrong assumption of the Rayleigh backscatter coefficient used to correct the overall lidar backscatter coefficient. A series of flights was conducted from Longyearbyen (Svalbard) across the western Arctic to Barrow (Alaska), reaching Station Nord (Greenland), Alert, NP-36 (at 88° 40′ N latitude), Eureka, Resolute Bay, Sachs Harbor, Inuvik, and Fairbanks, while complementary ground-based lidar measurements were regularly conducted at Ny-Ålesund, Eureka and Barrow (Stone et al., 2010). Significant aerosol backscatter and extinction effects were measured over the entire region, mainly caused by haze particles with diameters ranging from 0.13 to 0.20 μm. The PAMARCMiP lidar measurements showed that the aerosol extinction coefficient decreased in general with height from the surface to the top-level of the thermal inversion layer, found to be on average equal to 4 km, and often presented a secondary peak above. A second PAMARCMiP airborne campaign was conducted with the Polar 5 aircraft during April 2011, following the route from Longyearbyen to Barrow, flying over Station Nord, Alert, Eureka, Resolute Bay and Inuvik (Herber et al., 2012). During both campaigns, black carbon was observed at all altitudes sampled but at relatively low concentrations compared with historical values.

A climatological study of Arctic aerosols was made by Devasthale et al. (2011) examining the CALIOP measurements recorded from June 2006 to May 2010. The study showed that the bulk of the aerosol particles are confined within the first 1000 m of the troposphere, from about 65% of cases in winter to 45% in summer, while the rest is mainly suspended within the middle troposphere, at altitudes ranging from 3 to 5 km, especially in spring. The relative occurrences of aerosol types in the vertical profiles show that clean continental aerosol is the largest contributor in all seasons except in summer, while polluted continental aerosols are the second largest contributor to the total number of observed aerosol layers in winter and spring, and clean marine aerosol is the second largest contributor in summer and autumn. The average vertical profile of aerosol extinction coefficient was found to exhibit a pronounced peak at heights of about 0.4–0.7 km. Associated with the intrusions from mid-latitudes, polluted continental and smoke aerosols presented much broader distributions of optical and geometrical thicknesses, appearing to be more often optically thicker and higher up in the troposphere.

5. Airborne and satellite measurements

5.1. Basic remarks

Airborne sun-photometry employs ground-based techniques adapted to the special requirements (notably solar tracking) of an aircraft environment. Relatively frequent measurements can be made during ascending or descending profiles to achieve vertically stratified AOT measurements, which are sensitive to the aerosol vertical structure and can be converted to volume extinction coefficient profiles, which are analogous to the aerosol backscatter coefficient profiles derived from lidar measurements and shown in Fig. 16 (see Section 4). It is also possible to carry out measurements onboard airplanes flying above and below pollution plumes. These aircraft measurements offer the possibility of surveying large areas in relatively short time-periods, which is not possible, e.g., for ship-borne measurements. In particular, airborne measurements of this kind were made during the PAMARCMiP airborne campaign of April 2009 (Stone et al., 2010), in which various airborne lidar systems and a multi-wavelength sun-photometer were mounted onboard the AWI Polar 5 research aircraft to perform numerous measurements of volume aerosol scattering and extinction coefficients were conducted over the wide area from Svalbard across the western Arctic to Barrow, from the European to the Alaskan Arctic, and from sub-Arctic latitudes to near the Pole. The sun-photometer measurements were performed using a 8-channel sun-photometer system manufactured by NOAA/GMD (Boulder, Colorado, USA) in cooperation with ISAC-CNR (Bologna, Italy), and equipped with narrow-band visible and near-IR channels centred at wavelengths ranging from 0.355 to 1.064 μm, while the lidar measurements were conducted using a pair of downward-looking lidars, a depolarisation aerosol lidar and a tropospheric ozone DIAL. Additional independent in-situ measurements of particle size-distribution were also made onboard the AWI Polar 5 aircraft, and light extinction data were derived from the airborne lidar measurements to investigate the spectral effects produced by haze particles.

The measurements revealed that the spatial variations in $\tau(\lambda)$ observed during the most turbid period of the 2009 haze season were closely related to the atmospheric circulation patterns regulated by a dominant airflow from Eurasian anthropogenic sources. In addition, lidar observations showed the presence of elevated aerosol layers, as shown at Ny-Ålesund by Treffeisen et al. (2007) in early May 2006 during a transport event of biomass burning aerosols from agricultural fires in eastern Europe, and by Stock et al. (2012) in March 2008 during a BFF smoke pollution event over the European Arctic region.

Background values of τ(0.50 μm) not exceeding 0.06 were determined in the most remote areas, while haze values of τ(0.50 μm) varying from 0.12 to around 0.35 were measured, with the highest values found in the Beaufort Sea region towards the end of April. Such values of $\tau(\lambda)$ were anomalously high compared with those measured in the previous three years, because of the transport of haze particles from the industrial regions in Europe and Northern Asia. Arctic haze particles were frequently found to be concentrated within and just above the surface-based temperature inversion layer, showing in general bimodal size-distribution features, consisting of an accumulation mode of moderately small (water-soluble) particles and an additional mode mainly composed of insoluble coarse particles. In addition, the in-situ sampling and optical measurements revealed a marked decrease in the mean particle size with increasing altitude from the surface to 4 km, yielding values of the Ångström exponent α(0.412–0.675 μm) varying from 1.40 to 1.70. The airborne measurements showed that black carbon (BC) was highest near the North Pole, suggesting long-range transport

from combustion sources. However, the BC concentration measurements performed near the surface were nearly an order of magnitude lower than those reported from similar campaigns in the 1980s. Enhanced opacity at higher altitudes during the campaign was attributed to an accumulation of industrial pollutants in the upper troposphere, consisting of residual aged aerosol and soot particles originating from coal burning in China, in combination with volcanic aerosol resulting from the March–April 2009 eruptions of Mount Redoubt in Alaska and perhaps minor contributions from aircraft emissions. The Arctic haze particles observed during April 2009 were estimated to have reduced the net short-wave irradiance by − 2 to − 5 W m^{-2}, resulting in a slight cooling of the surface. Examining the data recorded during the second PAMARCMiP airborne campaign in April 2011, and some aerosol measurements coordinated with satellite flyovers of NASA's CALIPSO mission, Herber et al. (2012) found that such satellite-borne data can be useful to validate aerosol retrievals from the lidar and sun-photometer measurements made onboard the Polar 5 aircraft.

Even larger areas than those covered by airborne sun-photometer campaigns can be monitored by means of satellite observations. The retrieval of aerosol properties from satellite-based measurements is an ill-posed problem. The satellite retrieved aerosol optical thickness over bright surfaces such as snow and ice is often biassed and leads to errors when estimating aerosol-radiation interactions (IPCC, 2013). Polar-orbit satellite-mounted sensors like MODIS (Moderate Resolution Imaging Spectroradiometer) and MERIS (Medium Resolution Imaging Spectrometer) utilise multi-spectral information to characterise surface properties. The NASA/MODIS "dark-target" (DT) approach developed for the retrieval of aerosol properties uses the 2.1 μm band to estimate the reflectance in visible bands (Kaufman et al., 1997). The empirical relationships between the surface reflectance of visible channels and 2.1 μm channel were improved by considering the effect of geometry and surface types (Levy et al., 2007), while information on global aerosol properties was determined as a function of location and season by performing cluster analysis of in-situ measurements (Levy et al., 2010). The major limitation of the MODIS DT algorithm is that no retrievals are performed when the surface reflectance of the 2.1 μm channel is higher than 0.25 (Levy et al., 2007). For the retrieval over bright surfaces, such as desert and urban regions, Hsu et al (2004) developed the Deep Blue (DB) algorithm utilizing the fact that the surface is much darker in the short blue spectral channels compared with longer wavelengths. The second generation of DB algorithm, the so-called Enhanced Deep Blue algorithm, improved estimates of the surface reflectance, aerosol model selection and cloud-screening schemes (Sayer et al., 2012; Hsu et al., 2013). The current MODIS Collection 6.0 AOT product is created from three separate retrieval algorithms for different surface types (Levy et al., 2013): they are two DT algorithms for dark ocean surface as well as the vegetated/dark-soiled land and a DB algorithm over desert/arid land. MODIS Collection 6 also provides a 3 km AOT product compared to Collection 5 (Remer et al., 2013). The Bremen AErosol Retrieval (BAER) algorithm for MERIS (von Hoyningen-Huene et al., 2003, 2011) utilises the Normalized Difference Vegetation Index (NDVI). Polar-orbit satellites with multi-view observations such as AATSR (Advanced Along Track Scanning Radiometer) (Curier et al., 2009) and MISR (Multi-angle Imaging Spectroradiometer) (Diner et al., 2005a) make use of the Bidirectional Reflectance Distribution Function (hereinafter referred to as BRDF) surface properties to constrain the ill-posed inverse problem. A time series method is the most popular aerosol retrieval method for geostationary satellite based on the assumption that the surface reflectance does not change significantly during a short period of time (Knapp et al., 2002; Govaerts et al., 2010; Mei et al., 2012). The retrievals based on POLDER (Polarization and Directionality of the Earth's Reflectances) (Deuzé et al., 2001; Dubovik et al., 2011) intensity and degree of polarisation measurements provide more accurate AOT products with the advantage that the contribution of land surfaces to the degree of polarisation at the TOA is generally smaller in the visible as compared to the contribution of the underlying surface to the light intensity as measured on a satellite.

Among the various satellite-based observations, those provided by MODIS (Justice et al., 1998) mounted on the Terra and Aqua platforms are particularly useful for evaluating the AOT features in the polar regions, over the ocean and ice-free land surfaces, and studying aerosol climatology associated with the sources, transport and sinks of specific aerosol types (e.g., sulphates and biomass burning smoke particles). The twin MODIS sensors have been flying on the Terra platform since 2000 and on the Aqua platform since 2002, giving a large data-set of aerosol products using a number of algorithms over the past decades to retrieve columnar aerosol parameters over sea and land (Kaufman et al., 1997; Tanré et al., 1997; Hsu et al., 2004; Remer et al., 2005; Levy et al., 2013; Xue et al., 2014). To define the average seasonal maps of τ(0.55 μm), we downloaded data-sets of MODIS/Terra and MODIS/Aqua monthly Level-3 data (Atmosphere Monthly Global 1 × 1 Degrees Products MOD08_M3.051 and MYD08_M3.051, for the Terra and Aqua platforms, respectively) from the Giovanni website (http://disc.sci.gsfc.nasa.gov/giovanni). These had been collected for cloud-free atmospheric conditions over the eight years from January 2005 to December 2012, at Arctic latitudes ≥ 67° N and Antarctic latitudes ≥ 62° S. The cloud-screened Arctic AOT data-set was divided into seasonal sub-sets of τ(0.55 μm) for spring (March to May) and summer (June to August), separately for Terra and Aqua observations. The seasonal average maps of Level-3 AOT τ(0.55 μm) derived from MODIS/Aqua and MODIS/Terra are separately shown in Fig. 20, for 1° × 1° pixels over oceans and land areas not covered by snow and ice. The values of τ(0.55 μm) in the summer months are mainly lower than 0.15, with some areas characterised by average values ranging from 0.15 to 0.30 over the Central and Western Siberian Sea, and the Chukchi Sea, as well as over the Beaufort Sea, presumably due to the transport of BFF aerosol from Siberia and North America, respectively. The spring average values of τ(0.55 μm) range mainly from 0.10 to 0.25, with peaks of more than 0.30 in the Siberian, North American and North European sectors, associated with dense Arctic haze transported from the anthropogenic mid-latitude sources. These findings closely agree with the results obtained from the ground-based sun-photometer measurements conducted at coastal sites (Fig. 8a) and from the ship-borne AERONET/MAN measurements (Fig. 8b). Fig. 20 also shows that AOT cannot be retrieved from the MODIS data using the operational MODIS algorithm over Greenland and the North Pole in both spring and summer, and over large regions of Northern America and Siberia in spring, because of the high reflectance of the surfaces covered by sea ice and snow and also because of generally small values of AOT in these areas.

Reliable maps of exponent α cannot be retrieved from MODIS data over both land and ocean surfaces because of the low values of AOT in the polar regions and the relevant uncertainties affecting the MODIS aerosol products (Mishchenko et al., 2010; Kahn et al., 2011). In particular, Levy et al. (2013) determined the Collection 6 MODIS aerosol products to retrieve AOT and aerosol size-parameters from MODIS-observed spectral reflectance data and found that the Ångström exponent product over land cannot be reliably used. These findings were confirmed by Mielonen et al. (2011) who stated that MODIS data do not provide quantitative information about aerosol size and parameter α over land. Similarly, as a result of a validation study of Collection 5 MODIS Level-2 Aqua and Terra AOT and α products over ocean, Schutgens et al. (2013) found that these products exhibit significant biases due to wind speed and cloudiness of the observed scene, being significantly affected by AOT and α random errors due to cloud fraction contributions.

On the basis of these results, we have decided to examine here only the MODIS AOT data and exclude from the present analysis the MODIS α products obtained over snow- and ice-free land and ocean regions, since they were presumably affected by considerable uncertainties arising from: (i) the presence of cloud-fractions within the 1° × 1° pixels that cannot be correctly evaluated, and (ii) the variability of AOT at visible

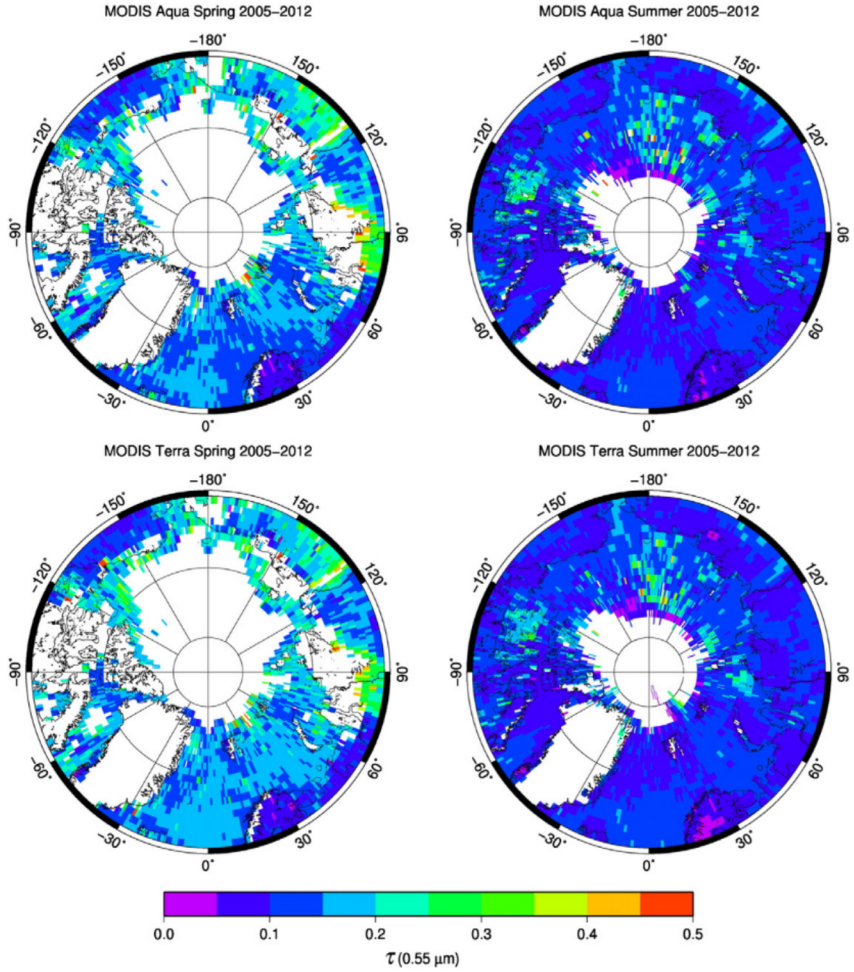

Fig. 20. Arctic maps of the seasonal average Level-3 aerosol optical thickness τ(0.55 μm) derived from MODIS/Aqua (upper part) and MODIS/Terra (lower part) satellite data recorded from 2005 to 2012 during the spring (left-hand side) and summer (right-hand side) 3-month periods.

and near-infrared wavelengths, due to cloud extinction effects, which may efficiently contribute to lower exponent α. On the basis of the AERONET/MAN measurements, this parameter was evaluated to range from less than 1.00 to around 1.75 over the Arctic Ocean sectors in spring and summer, and from less than 0.50 to about 2.00 in Antarctica, with in general lower values over the off-shore areas far from the Antarctic coasts.

The Antarctic aerosol data-set downloaded from the Giovanni website over the latitude range ≥ 62° S covers not only the land region of the Antarctic continent but also the off-shore ocean areas no further than 1000 km from the coasts. Only the MODIS/Aqua and MODIS/Terra data collected from December to February were separately examined to determine the maps of average τ(0.55 μm), limited in practice to the oceanic areas only (Fig. 21). The results indicate that such seasonal average values of τ(0.55 μm) are lower than 0.10 over all ocean areas close to the Antarctic coasts and sometimes can exceed 0.10 over the off-shore areas, in close agreement with the values derived from ground-based sun-photometer measurements at coastal Antarctic sites (Fig. 13a) and from AERONET/MAN measurements (Fig. 13b).

Fig. 21 also shows that no useful information is available from MODIS observations over the interior of Antarctica when using the traditional retrieval procedures. The retrieval of $\tau(\lambda)$ over a bright surface is indeed a very difficult task, because it is hard to separate the radiance contributions by the reflecting surface and atmospheric aerosol backscattering to the overall radiance observed by a satellite-borne sensor at the TOA-level, especially for the very large solar zenith angles typical of polar latitudes. Mei et al. (2013a) overcame the above difficulties by following a synergetic approach based on the use of both MODIS/Terra and MODIS/Aqua data, together with: (i) the a-priori assumption of aerosol optical parameters retrieved over snow made with the Aerosol Properties Retrieval over Snow (APRS) algorithm, and (ii) an appropriate model of the BRDF reflectance representing snow-covered surfaces. The APRS algorithm was based on the operational bi-angle approach proposed by Xue and Cracknell (1995) to retrieve non-absorbing